Chinese Journal of Chemical Engineering 94 (2026) 44–59

Contents lists available at ScienceDirect

Chinese Journal of Chemical Engineering

journal homepage: www.elsevier.com/locate/CJChE

Full Length Article

Mechanism and performance of Fluoride's removal using hydrochar modified by different loadings of aluminum source

Fuqiang Xu [1], Miao Gong [1, 2, *], Piao Liu [1], Qiao Xu [1], Ying Su [3], Yujie Fan [4], Shuai Guo [1, *]

[1] School of Civil Engineering, Hefei University of Technology, Hefei 230009, China
[2] Anhui Provincial Engineering Laboratory for Rural Water Environment and Resources, Hefei 230009, China
[3] College of Civil Engineering, Yancheng Institute of Technology, Yancheng 224051, China
[4] School of Civil Engineering, Nanyang Institute of Technology, Nanyang 473004, China

ARTICLE INFO

Article history:
Received 28 September 2025
Received in revised form
16 December 2025
Accepted 24 December 2025
Available online 14 March 2026

Keywords:
Sewage sludge
Hydrothermal carbonization
Aluminum-loaded hydrochar
Adsorption
Defluoridation
Waste treatment

ABSTRACT

The present study prepared aluminum-functionalized hydrochars through a single-step hydrothermal carbonization reaction of sewage sludge using various Al precursors (namely $AlCl_3$, $Al_2(SO_4)_3$, $Al(NO_3)_3$, $Al(OH)_3$, and Al_2O_3). We found that ligand properties and hydrolysis pathways determine the formation of $Al(OH)_3$/AlOOH and low-reactivity Al_2O_3 regions, thereby regulating the density and accessibility of surface Al—OH sites and thus affecting fluoride binding. X-ray photoelectron spectroscopy (XPS) analysis revealed that Cl^-, by forming $[AlCl(H_2O)_5]^{2+}$ species through coordination, retarded the hydrolysis kinetics and promoted the synergistic formation of $Al(OH)_3$ (39.04%) and AlOOH (47.52%). Conversely speaking, SO_4^{2-} induced the oriented growth of layered hydroxides through a templating effect, while the weak coordination capability of NO_3^- led to dehydroxylation and the predominant formation of inert Al_2O_3 (20.92%) with low —OH functionality. Under optimized conditions (30% $AlCl_3$), organic decomposition increased BET surface area to 111.54 $m^2 \cdot g^{-1}$ (44% over unmodified hydrochar), yielding Langmuir capacity of 24.10 $mg \cdot g^{-1}$ (10-fold enhancement) *via* pseudo-second-order kinetics and Freundlich isotherms. Fluoride sequestration primarily occurred through hydroxyl-fluoride ligand exchange, which was augmented by electrostatic interactions and mesoporous confinement. The hydrochar retained 70% capacity over five cycles, with anion interference followed the order: $SO_4^{2-} > NO_3^- > PO_4^{3-} > Cl^-$. These findings highlight the potential of aluminum-modified hydrochar for efficient removal of fluoride from aqueous solutions and resource valorization of sewage sludge.
© 2026 The Chemical Industry and Engineering Society of China, and Chemical Industry Press Co., Ltd. All rights are reserved, including those for text and data mining, AI training, and similar technologies.

1. Introduction

In China, rapid urbanization has led to the generation of approximately 14 million tons (dry mass) of sewage sludge per year [1]. Traditional disposal methods face multiple challenges. For example, landfills lead to leachate pollution and emissions of methane [2]. Incineration can produce dioxin emissions as high as 2.11×10^{-2}–41.86 $ng \cdot m^{-3}$ I-TEQ [3]. Similarly, composting results in products that still contain large quantities of antibiotics and antibiotic resistance genes (ARGs), posing ecological risks [4]. Against this backdrop, hydrothermal carbonization (HTC; 180–260 °C, 2–10 MPa) utilizes subcritical water to mediate hydrolysis-polycondensation reactions, converting sludge into hydrochar that is rich in mesopores (2–50 nm) and oxygen-containing functional groups (—COOH, and —OH) [5]. Compared to traditional treatment methods, hydrothermal carbonization has the advantages of higher energy efficiency and lower emissions of greenhouse gases, with an energy recovery rate that is 11 times higher than that of landfills with 78% to 85% lower emissions of greenhouse gases [6]. Due to its tunable surface chemistry and porous structure, sludge-derived hydrochar has emerged as an efficient and low-cost adsorbent, with broad applications in treating wastewater containing heavy metals, removal of organic pollutants, and purification of gases. For instance, the adsorption capacities of sludge hydrochar for methylene blue and rhodamine B have been reported to be 80.00 $mg \cdot g^{-1}$ and 18.37 $mg \cdot g^{-1}$, respectively [7,8].

* Corresponding authors.
E-mail addresses: miaogong@hfut.edu.cn (M. Gong), guoshuai@hfut.edu.cn (S. Guo).

https://doi.org/10.1016/j.cjche.2025.12.047
1004-9541/© 2026 The Chemical Industry and Engineering Society of China, and Chemical Industry Press Co., Ltd. All rights are reserved, including those for text and data mining, AI training, and similar technologies.

Fluoride pollution poses a critical risk to worldwide drinking water security. Data from the United Nations' Environment Programme indicate that over 200 million individuals are at risk from water exceeding the limit of 1.5 $mg \cdot L^{-1}$ fluoride, with endemic fluorosis rates reaching 12% to 15% in affected areas [9]. The primary sources of fluoride pollution include industrial emissions (such as aluminum electrolysis, production of phosphate fertilizer, and manufacturing of solar photovoltaic cells), fluorite mining, and the overuse of fluoride-containing pesticides [10,11]. Reported fluoride levels in seawater, surface freshwater and groundwater span 0.9–1.4 $mg \cdot L^{-1}$, 0.01–3 $mg \cdot L^{-1}$, and 1–35 $mg \cdot L^{-1}$, respectively, often surpassing the World Health Organization's guideline of 1.5 $mg \cdot L^{-1}$ for potable water [12]. Long-term consumption of high-fluoride water not only affects the health of bones but may also increase the risk of neurological damage and cognitive impairment, underscoring the urgent need for effective remediation strategies for fluoride-contaminated waste streams.

Different treatment techniques are used for different concentrations of fluoride contamination. Chemical precipitation is mainly used for high concentrations of fluoride (>10 $mg \cdot L^{-1}$). Aluminum salts or lime rapidly reduce fluoride concentrations, but have limited effect when fluoride is present in trace amounts (<2 $mg \cdot L^{-1}$) [13]. Adsorption has emerged as the preferred method for treating waste streams with low levels of fluoride contamination due to its operational simplicity, affordability, and selectivity. However, unmodified hydrochar showed significant limitations in adsorbing fluoride ions (F^-), with a low isoelectric point (pH_{zpc} of around 5.43) and negative charge under typical aquatic pH conditions (6.5–8.5), thus fostering electrostatic repulsion with F^- and diminishing the adsorption efficiency [14,15].

Modification of adsorbents by loading metals onto them has proven to be an effective strategy to overcome some of the limitations of conventional adsorbents [5]. In particular, aluminum-based materials offer significant advantages due to their abundant natural occurrence, strong ability to coordinate with fluoride, and multiple morphological forms (AlOOH, Al_2O_3, and $Al(OH)_3$). Fluoride sequestration by these forms primarily involves Al—F complexation through ion exchange and electrostatic forces [16]. However, the removal of fluoride varies greatly among various aluminum-based adsorbents. Among them, $Al(OH)_3$ has the most favorable fluoride removal effect due to its higher concentration of Al—OH bonds, followed by AlOOH, and Al_2O_3 [17]. However, AlOOH is more resistant to pH changes in water and has good fluoride removal performance over a wide pH range [18]. Previous studies have shown that constructing AlOOH nanosheets on biochar through hydrothermal methods can increase the maximum Langmuir F^- adsorption capacity to 41.9 $mg \cdot g^{-1}$ and maintain >85% removal efficiency over a wide range of pH (4.5–10.5) [19].

Conventional methods for implementing aluminum modification mainly include multi-step processes such as impregnation, co-precipitation and sol-gel methods. For instance, aluminum/yttrium-doped sludge biochar (Al/Y-CSBC) exhibited expanded surface area, elevated pH_{zpc} (9.14), 62.44 $mg \cdot g^{-1}$ adsorption capacity, and 95% retention of initial adsorption capacity after six cycles [20]. However, conventional modification methods have obvious drawbacks. They require multiple steps (pre-carbonization, loading, and secondary carbonization), consume high amounts of energy, and often lead to uneven distribution of metal and leaching problems [21].

Despite the promise of aluminum modification for enhancing hydrochar's fluoride affinity, systematic studies on the mechanism and performance of aluminum loading onto sludge-derived hydrochar remain scarce in the literature, with most efforts limited to multi-step processes on biochar rather than hydrochar [19,22,23]. Critically, no prior work has explored the effects of one-step loading using different aluminum sources (*e.g.*, $AlCl_3$, $Al_2(SO_4)_3$) on adsorption performance, nor delineated how precursor chemistry influences Al^{3+} transformation and speciation ($Al(OH)_3$, AlOOH, Al_2O_3) in the hydrothermal environment, which is essential for rationally designing high-performance, waste-derived adsorbents and understanding surface complexation mechanisms in fluoride sequestration. Addressing these gaps is vital because it enables the development of simplified, scalable synthesis routes that leverage sewage sludge valorization while providing mechanistic insights to optimize Al—OH site density and accessibility for efficient defluoridation.

Based on the above analysis, the present study proposes an innovative method for preparing aluminum-loaded sludge-derived hydrochar. The method involves *in situ* loading of aluminum onto sludge-derived hydrochar through a one-step hydrothermal process, which simultaneously achieves chemical anchoring of aluminum species and modulation of porous structure during the carbonization of sludge. The proposed method avoids the complexity of conventional multi-step modifications, simplifies the process, and enhances the properties of the resulting material.

The present study aims at: (1) assessing the effects of various aluminum precursors ($AlCl_3$, $Al_2(SO_4)_3$, $Al(NO_3)_3$, $Al(OH)_3$, and Al_2O_3) on removing fluoride from aqueous streams; (2) analyzing the kinetics, thermodynamics, and factors affecting the adsorption of fluoride using aluminum-loaded hydrochar; (3) evaluating the recyclability of the proposed material; and (4) delineating the adsorption mechanism. The present study proposes an innovative one-step hydrothermal process for preparing aluminum-loaded sludge-derived hydrochar, which simultaneously achieves carbonization and *in situ* metal anchoring to simplify production and enhance uniformity compared to conventional multi-step methods. Beyond performance improvement, this work aims to provide novel mechanistic understanding of how aluminum precursor selection governs speciation ($Al(OH)_3$, AlOOH, Al_2O_3), surface hydroxyl chemistry, and fluoride complexation pathways.

2. Experimental

2.1. Materials and chemicals

Dewatered sewage sludge was sourced from the Hudaying wastewater treatment facility in Hefei, China. Part of the fresh sludge was collected for analyzing the composition and stored at <4 °C to maintain its original state. The detailed results are presented in Table 1. The rest was dried by air, milled to a fine powder, and stored for subsequent use.

All reagents used in the experiments were of analytical grade and purchased from Sinopharm Chemical Reagent Co., Ltd. (China).

2.2. Synthesis of aluminum-loaded sludge-derived hydrochar

The preparation conditions for obtaining aluminum-loaded hydrochar were optimized. Parameters were adjusted individually while holding others constant (as detailed in Table 2). According to the fluoride removal effect of hydrochar obtained under different conditions, the optimized preparation conditions were determined to be as follows: 180 °C, 1 h, 30% $AlCl_3$. Aluminum precursor loadings are expressed as weight percentage of the hexahydrate salt (*e.g.*, $AlCl_3 \cdot 6H_2O$) relative to dry sludge mass. For 30% $AlCl_3$, 2.1 g $AlCl_3 \cdot 6H_2O$ was blended with 7 g dewatered sludge (dry basis). The process employed a 100 ml Hastelloy C276 autoclave (Model MSI100-P7-T7-HC1-SV-R, Anhui Kemi Machinery

Table 1
Physicochemical properties of dewatered sewage sludge.

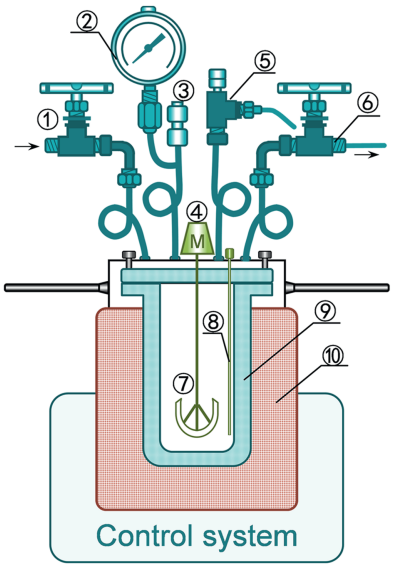
Moisture content[①]/% (mass)	Proximate analysis[①]/% (mass)			Ultimate analysis[①]/% (mass)					HHV[③]/MJ·kg^{-1}
	VM	FC	Ash	C	H	N	S	O[②]	
82.25 ± 0.15	53.12 ± 0.09	5.52 ± 0.15	41.36 ± 0.12	25.61	5.10	4.41	0.50	22.07	11.76

Note: VM, Volatile matter; FC, Fixed carbon.
① Estimated by air-dried basis.
② Estimated by difference (O% = 100%−ash%−C%−H%−N%−S%).
③ Higher heating value (HHV) calculated by Dulong's Formula, *i.e.*, HHV/(MJ·kg^{-1}) = 0.3393C + 1.443 (H—O/8)+0.0927S + 0.01494 N.

Table 2
Preparation conditions for aluminum-loaded hydrochar.

Investigated factor	Types of aluminum sources	Hydrothermal temperature/°C	Aluminum additions/% (mass)
Types of aluminum sources	$AlCl_3·6H_2O$, $Al_2(SO_4)_3·18H_2O$, $Al(NO_3)_3·9H_2O$, $Al(OH)_3$, Al_2O_3	180	30
Hydrothermal temperature	$AlCl_3·6H_2O$	180, 200, 220, 240, 260	30
Aluminum addition/%	$AlCl_3·6H_2O$	180	10, 20, 30, 40, 50

Technology Co., Ltd., China), as illustrated in Fig. 1. A blend comprising 7 g dewatered sludge, 2.1 g $AlCl_3·6H_2O$, and 45 ml ultrapure water was introduced into the sealed vessel. Timing commenced upon attaining the targeted temperature. For zero residence time, heating was stopped and the vessel was cooled to room temperature. The resultant solid was isolated through vacuum filtration, rinsed successively with absolute ethanol and ultrapure water until effluent clarity was achieved. The solid was then oven-dried at 105 °C to constant mass, pulverized, and passed through a 100-mesh (150 μm) sieve. The resulting product was designated as 180°C-1h-30%-$AlCl_3$.



① Inlet; ② Pressure gauge; ③ Explosion-proof valve; ④ Motor; ⑤ Safety valve; ⑥ Gathering valve; ⑦ Stirring paddle; ⑧ Thermocouple; ⑨ Reactor; ⑩ Furnace

Fig. 1. Schematic presentation of the experimental apparatus used.

2.3. Characterization

Physicochemical attributes of the aluminum-functionalized hydrochar were examined using multiple analytical techniques. Surface topography was visualized using field-emission scanning electron microscopy (Zeiss Gemini 500, ZEISS Sigma 360). Textural properties, including surface area and porosity, were quantified using N_2 adsorption-desorption isotherms (Autosorb-iQ3 analyzer), with BET modeling for surface area and DFT for pore metrics. Surface elemental speciation and oxidation states were examined using X-ray photoelectron spectroscopy (Thermo Scientific K_α). Crystalline phases were identified using X-ray diffraction (Rigaku SmartLab SE).

2.4. Adsorption of fluoride ions

Fluoride uptake was assessed using batch experiments under diverse conditions (summarized in Table 3). A stock solution of 20 mg·L^{-1} F^- was formulated using an appropriate amount of NaF, and 0.25 g hydrochar was dispersed in 100 mL aliquots, which were agitated at 25 °C for 12 h. After reaching equilibrium, filtration was performed prior to measurement of residual F^- (C_e). Equilibrium capacity (q_e) for fluoride's adsorption is given by Eq. (1).

$$q_e = \frac{(C_e - C_0) \times V}{m} \tag{1}$$

where q_e denotes the equilibrium uptake (mg·g^{-1}), C_0 represents the initial concentration (mg·L^{-1}), C_e represents the equilibrium concentration (mg·L^{-1}), V represents the volume of solution (L), and m represents the mass of the adsorbent (g).

The optimum hydrochar variant underwent further refinement of dosage and pH, followed by kinetic and isothermal analyses, alongside anion interference evaluations (Table 3).

Adsorption kinetic studies were conducted under optimal conditions (0.125 g adsorbent, 100 ml, 100 mg·L^{-1} F^-, pH 6 ± 0.2, 25 °C). Samples were taken at various time points (10–1440 min) to measure fluoride concentration and adsorption rates. Data were fitted to:

Pseudo-first-order:

$$\ln(q_e - q_t) = \ln q_e - k_1 t \tag{2}$$

Pseudo-second-order:

$$\frac{t}{q_t} = \frac{1}{(k_2 q_e)^2} \tag{3}$$

Intra-particle diffusion:

$$q_t = K_3 t^{0.5} + C \tag{4}$$

where q_t is uptake at time t (mg·g^{-1}); t is the adsorption time (min); k_1 (min^{-1}), k_2 (min^{-1}), and K_3 (mg·(g·h$^{0.5}$)$^{-1}$) are rate constants, and C is the boundary layer thickness.

Table 3
Parameters and their values used to study the adsorption of fluoride.

Experiment	Adsorbent dose/g	Adsorption solution volume/ml	Initial F^- concentration/ $mg \cdot L^{-1}$	pH range	Temperature/ °C	Contact time/h	Variables/notes
Initial screening	0.250	100	20	6 ± 0.2	25	12	Basic performance comparison
Dosage optimization	0.100 −1.000	100	100	6 ± 0.2	25	24	Dosages: 0.100, 0.125, 0.150, 0.175, 0.200, 0.225, 0.250, 0.500, 0.750, 1.000 g
pH optimization	0.125	100	100	2-11	25	24	pH adjusted with HCl or NaOH
Adsorption kinetics	0.125	100	100	6 ± 0.2	25	Up to 24	Samples taken at 10, 20, 30, 60, 90, 120, 180, 240, 360, 480, 720, 960, 1200, 1440 min
Adsorption thermodynamics	0.125	100	20, 30, 40, 50, 60, 80, 100	6 ± 0.2	25-45	24	Temperatures: 25, 35, and 45 °C
Anion coexistence experiments	0.125	100	100	6 ± 0.2	25	24	Anion types: Cl^-, NO_3^-, SO_4^{2-}, PO_4^{3-}; concentrations: 50, 100, 150 $mg \cdot L^{-1}$
Actual fluoride-containing wastewater	0.125	100	6.68	6.12	25	2	NO_3^-: 821.61 $mg \cdot L^{-1}$; SO_4^{2-}: 1446.49 $mg \cdot L^{-1}$; COD: 350 $mg \cdot L^{-1}$; Redox potential: −35 mV

Isotherm experiments involved 0.125 g hydrochar in 100 ml NaF solutions (20–100 $mg \cdot L^{-1}$ F^-, pH 6 ± 0.2) at 25, 35, and 45 °C for 24 h, fitted to:

Langmuir Isotherm:

$$q_e = \frac{q_{max} K_L C_e}{1 + K_L C_e} \quad (5)$$

Freundlich Isotherm:

$$q_e = K_F C_e^{1/n} \quad (6)$$

where q_{max} is saturation capacity ($mg \cdot g^{-1}$); K_L is Langmuir constant ($L \cdot mg^{-1}$); K_F is Freundlich constants ($(mg \cdot g^{-1}) \cdot (L \cdot mg^{-1})^{1/n}$), and n is heterogeneity factor.

Anion competition was probed by adding Cl^-, NO_3^-, SO_4^{2-}, or PO_4^{3-} (50–150 mL) to 100 mL of 100 $mg \cdot L^{-1}$ F^- (pH 6 ± 0.2, 25 °C, 24 h). All trials were triplicated, with averages reported.

2.5. Adsorption experiments using actual fluoride-containing wastewater and regeneration of hydrochar

The physicochemical properties of actual fluoride-containing wastewater are shown in Table 3. The adsorption performance of the proposed adsorbent was tested by dispersing 0.125 g hydrochar in 100 ml for 2 h at ambient temperature.

After each 24-h adsorption batch, the mixture was vacuum-filtered *via* a 0.45 μm PES membrane to separate spent hydrochar from supernatant; the retained solid is rinsed twice with 100 ml deionized water (pH 7.0) to remove residual ions without altering the surface Al speciation, then soaked in 50 ml of 0.5 $mol \cdot L^{-1}$ Na_2CO_3 for 4 h, rinsed again with 100 ml deionized water, and dried at 75 °C for 12 h to constant mass for the next cycle. This way, the proposed adsorbent was recycled and reused for five times, with retained adsorption efficiency (RE) computed as given by Eq. (7).

$$RE = \frac{q_n}{q_1} \times 100\% \quad (7)$$

where q_1 and q_n represent initial and post-cycle capacities ($mg \cdot g^{-1}$), respectively.

3. Results and Discussion

3.1. Effect of the type of aluminum precursor on the physicochemical properties and defluoridation efficiency of aluminum-loaded sludge-derived hydrochar

3.1.1. Effect of the type of aluminum precursor on defluoridation efficiency

As shown in Fig. 2(a), the adsorption performance of various hydrochars for F^- varied significantly with the type of aluminum source employed for adsorbent synthesis. When $AlCl_3$ was used, the hydrochar showed the highest adsorption capacity (3.45 $mg \cdot g^{-1}$), which was 29% and 238% higher than those observed for $Al_2(SO_4)_3$ (2.68 $mg \cdot g^{-1}$) and $Al(NO_3)_3$ (1.02 $mg \cdot g^{-1}$), respectively. In contrast, Al_2O_3 and $Al(OH)_3$-derived hydrochars showed no significant differences in terms of their F^- adsorption capacities. Therefore, $AlCl_3$ was selected as the preferred type of aluminum precursor for subsequent experiments.

The effect of the dosage of $AlCl_3$ on the adsorption capacity of F^- is illustrated in Fig. 2(b). Increasing the $AlCl_3$ loading from 10% to 30% increased the adsorption capacity from 1.04 $mg \cdot g^{-1}$ to 3.45 $mg \cdot g^{-1}$. Loadings of $AlCl_3$ that exceeded 30% yielded a progressive decline in adsorption capacity to 2.85 $mg \cdot g^{-1}$, confirming 30% loading of $AlCl_3$ as the optimum value. This phenomenon stems from pore blocking effects: although total aluminum content increases, the accessibility and reactivity of aluminum-hydroxyl sites diminish accordingly. A similar phenomenon was observed in the study by Olivares-Marin *et al.*[24], where the amount of aluminum added increased from 5:3 to 10:3 (Al to biomass ratio), resulting in a decrease in specific surface area from 38 $m^2 \cdot g^{-1}$ to 35 $m^2 \cdot g^{-1}$. This trend is consistent with our subsequent BET characterization results . Furthermore, Fig. S1(d) shows that although the amount of aluminum added during the experiment was increased (30% to 50%), the actual aluminum content loaded onto the hydrochar did not increase (12.3% (mass) Al to 11.7% (mass) Al). The role of hydrothermal temperature in defluoridation is shown in Fig. 2(c). For unmodified hydrochar, the adsorption capacity diminished from 2.34 $mg \cdot g^{-1}$ to 0.68 $mg \cdot g^{-1}$, followed by a minor recovery to 0.85 $mg \cdot g^{-1}$, which stabilized once the temperature went beyond 200 °C. In contrast, aluminum-loaded hydrochar showed maximum capacity at 180 °C (3.45 $mg \cdot g^{-1}$, 47% enhancement over pristine hydrochar). Compared to pristine hydrochar, notable

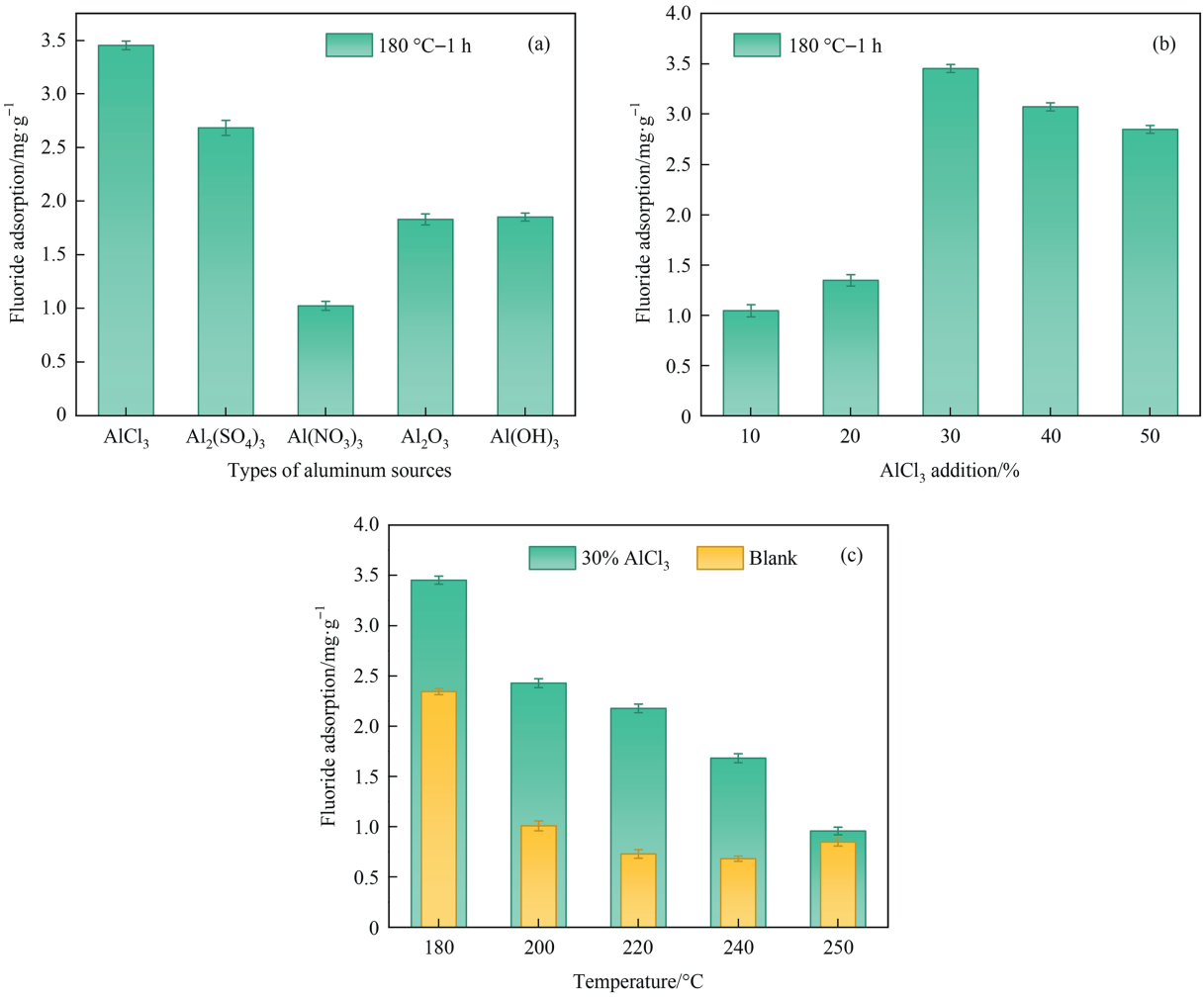


Fig. 2. Effect of (a) type of aluminum precursor, (b) aluminum chloride additions, and (c) hydrothermal temperature on the fluoride removal performance at 180 °C.

improvements in adsorption capacity occurred at 200 °C (141%), 220 °C (199%), and 240 °C (147%). The hydrothermal synthesis temperature controls the formation of aluminum morphology and the accessibility of pores, with 180 °C being the optimal hydrothermal preparation temperature. In general, hydrochar prepared under low-temperature conditions contain more active sites and have a higher specific surface area. As the hydrothermal temperature increases, the degree of carbonization rises, and the number of active sites decreases. Additionally, pore collapse reduces the specific surface area, leading to a decline in adsorption performance [5]. This was also confirmed in subsequent characterizations.

3.1.2. Effect of the type of aluminum precursor on the physicochemical properties of the adsorbent

To investigate the effects of the type of aluminum precursor, its dosage, and hydrothermal temperature on aluminum speciation, XPS was used to characterize the surface chemical composition and electronic structure of aluminum-loaded hydrochars. The high-resolution Al 2p spectra of hydrochars prepared under various conditions, including those after adsorbing fluoride, are shown in Fig. 3. Three aluminum species including Al_2O_3, $Al(OH)_3$ and AlOOH were identified, with their characteristic binding energies at 74.1, 74.8, and 75.2 eV, respectively.

Fig. 3(a)–(e) show the high-resolution Al 2p XPS spectra of aluminum-loaded hydrochars prepared using different precursors. Different aluminum precursors yielded distinct speciation patterns under hydrothermal conditions. At 180 °C with 30% loading of $AlCl_3$ (Fig. 3(a)), Cl^- formed $[AlCl(H_2O)_5]^{2+}$ complexes, slowing the kinetics of hydrolysis and resulting in the relative contents of 39.04% for $Al(OH)_3$ and 47.52% for AlOOH [25]. This observation aligned with classical hydrolysis-condensation theory, where complex formation modulates the activation energy barrier of hydrolysis reactions. Compared to dehydroxylation, a preference exists for hydroxyl-rich phases. For instance, in the distribution of aluminum(III) species in aqueous solutions,chloride ions enhance surface hydroxyl density by stabilizing complexes [26]. For $Al_2(SO_4)_3$ (Fig. 3(b)), SO_4^{2-} exhibited a dual mechanism. It not only suppressed the initial rate of hydrolysis for Al^{3+} through strong coordination but also guided the oriented growth of layered hydroxides through a template effect [27,28]. Similar to sulfate-guided boehmite assembly in calcium-aluminum layered double hydroxide fluoride removal systems, this process enhances phase ordering and anion tolerance [29]. Consequently, the material was significantly enriched in $Al(OH)_3$ (44.29%) and AlOOH (52.72%), with only 2.99% Al_2O_3 present in it. For $Al(NO_3)_3$ (Fig. 3(c)), weak NO_3^- coordination failed to stabilize intermediates, promoting the dehydroxylation of $Al(OH)_3$ and AlOOH under high-temperature conditions and resulting in 20.92% Al_2O_3 [28]. For $Al(OH)_3$ precursor (Fig. 3(e)), partial dehydration led to the formation of AlOOH (29.85%) and Al_2O_3 (48.53%), indicating the coexistence of physical mixing and reconstruction of the surface. For Al_2O_3 (Fig. 3(d)), the precursor was largely inert to the

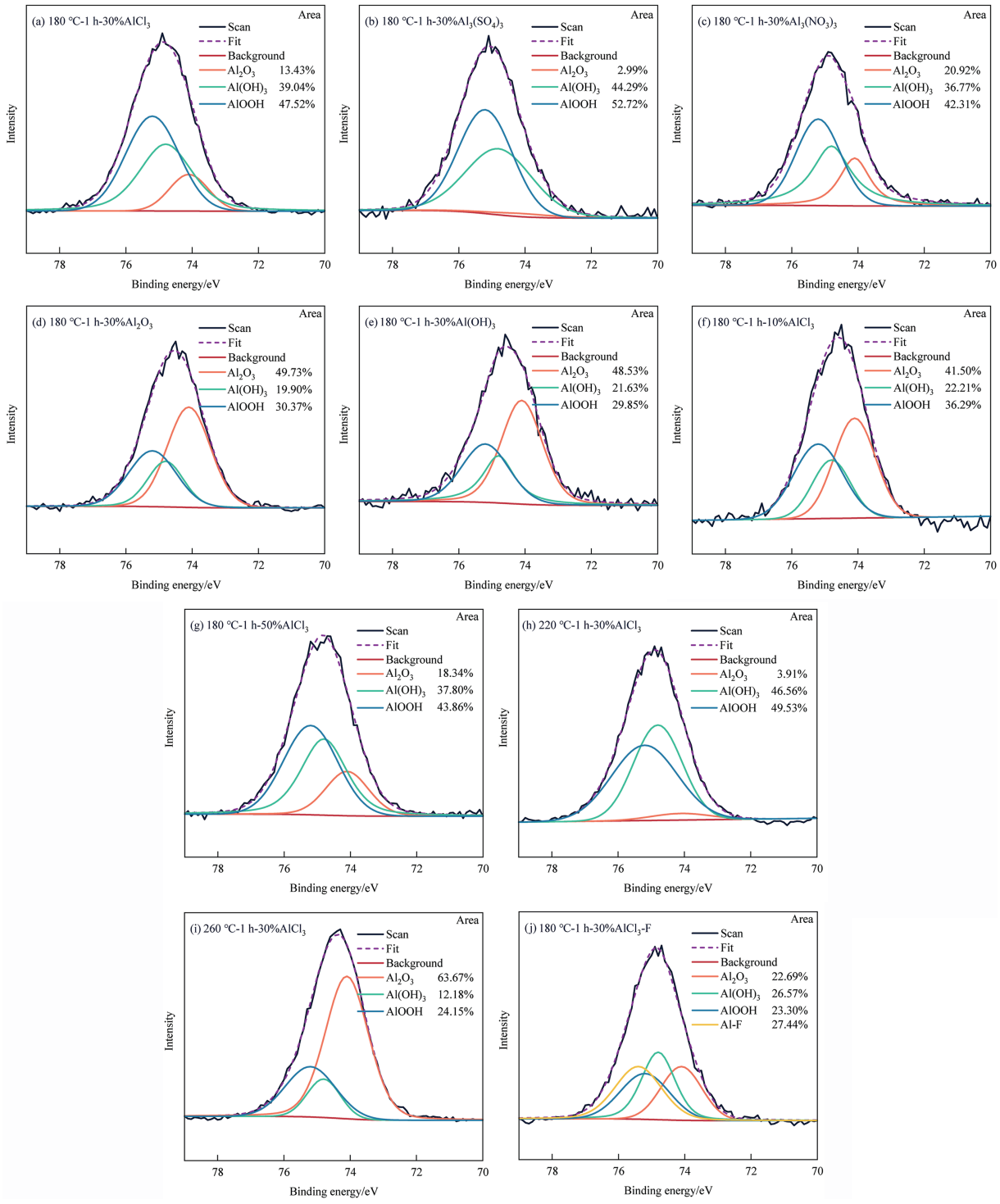


Fig. 3. XPS Al 2p spectra of hydrochar prepared under (a–e) different aluminum precursor loadings, (f, g) different $AlCl_3$ loadings, (h, i) different hydrothermal temperatures and (j) hydrochar after adsorption of F^-.

hydrothermal process, and accounted for as much as 49.73% of the total content of aluminum. The remaining aluminum species may have been derived from the aluminum contained in the sludge itself.

Fig. 3((a), (f)–(g)) show the Al 2p spectra of hydrochars with different loadings of $AlCl_3$. Varying the dosage of $AlCl_3$ impacted the speciation of aluminum. At 10% loading (Fig. 3(f)), the concentration of Al^{3+} in the solution was insufficient to form a continuous hydrolysis-condensation network, and instead triggered non-classical crystallization pathways through local supersaturation, which led to a sharp increase in the content of Al_2O_3 to 41.50% [30]. For 50% loading of $AlCl_3$ (Fig. 3(g)), intensified hydrolysis and high ionic strength facilitated the formation of polymeric aluminum species such as $[Al_{13}O_4(OH)_{24}(H_2O)_{12}]^{7+}$ [30]. This intermediate was gradually converted to $Al(OH)_3$ (37.80%) and AlOOH (43.86%), whereas it suppressed the formation of Al_2O_3

(18.34%). At the hydrothermal temperature of 220 °C (Fig. 3(h)), $Al(OH)_3$ underwent dehydration to AlOOH, raising its proportion to 49.53%. At the hydrothermal temperature of 260 °C (Fig. 3(i)), AlOOH was dehydroxylated to thermodynamically stable Al_2O_3 (63.67%) [31]. The resulting low surface hydroxyl density led to reduced adsorption activity. This finding was consistent with surface coordination chemistry theory that states that oxygen vacancies on Al_2O_3 preferentially form monodentate complexes with H_2O, whereas the bridging hydroxyls of AlOOH are more likely to form bidentate complexes with adsorbates [32].

Although Al 2p peak separation indicates that the relative fractions of $Al(OH)_3$ and AlOOH increases under some conditions, the fluoride uptake does not scale with these surface fractions alone. In practice, capacity follows the "accessible —OH density", which depends jointly on (i) the abundance and identity of reactive phases ($Al(OH)_3$, AlOOH), (ii) the external and internal surface area, (iii) the openness and continuity of mesopores that control site accessibility and diffusion, and (iv) the extent to which terminal *versus* bridged —OH groups are presented to solution. Consequently, a specimen may show a higher XPS-visible $Al(OH)_3$+AlOOH fraction yet deliver lower uptake if a portion of these hydroxyls is buried under thicker hydrated overlayers or resides in constricted pores over the experimental contact time window.

Fig. 3((a), (j)) compare the Al 2p spectra of aluminum-loaded hydrochar before and after the adsorption of fluoride. After the adsorption, four peaks appeared in the spectrum (Fig. 3(j)), including a new peak at 75.4 eV, which was assigned to Al-F bonds and confirmed the chemisorption of fluoride on the surface of hydrochar [33]. Moreover, the proportions of $Al(OH)_3$ and AlOOH decreased from 39.04% to 47.52% to 26.57% and 23.30%, respectively, while that of Al_2O_3 increased from 13.43% to 22.67%. The reductions in contents of $Al(OH)_3$ and AlOOH confirmed their pivotal role in the removal of fluoride by hydrochar. The —OH groups played a crucial role in the defluoridation process. Fluoride (F^-) underwent ion exchange with —OH [14,33], whereas the surface —OH groups on aluminum-loaded hydrochar could also participate in the removal of fluoride through hydrogen bonding interactions [34]. To further confirm the role of surface hydroxyl groups in fluoride sequestration, ATR-FTIR analysis was performed on the optimal Al-loaded hydrochar before and after adsorption (Fig. S4). The pre-adsorption spectrum exhibited a broad OH stretching band at 3000–3600 cm^{-1}, characteristic of Al—OH and residual hydrochar hydroxyls. Post-adsorption, the intensity of the 3000–3600 cm^{-1} band markedly decreased, indicating consumption of surface hydroxyls *via* ligand exchange. These spectral changes corroborate the XPS evidence of Al—OH sites involvement and support the proposed mechanism of hydroxyl-mediated fluoride uptake on the Al-functionalized hydrochar surface.

Overall, the precursor-dependent hydrolysis and speciation of aluminum directly governed the physicochemical properties of the sludge-derived hydrochar. This demonstrates the importance of selecting appropriate aluminum precursors to optimize the outcomes from hydrothermal carbonization and design high-performance aluminum-loaded sludge-derived hydrochars for efficient removal of fluoride from aqueous streams.

The nitrogen adsorption-desorption isotherms (Fig. 4) demonstrated that both pristine and aluminum-loaded hydrochars exhibited typical Type IV isotherms along with H3 hysteresis loops, signifying the presence of multilevel mesoporous architectures (2–50 nm) [20]. Parameters related to the porous structure under various preparation conditions are summarized in Table 4. At the hydrothermal temperature of 180 °C, the amount of aluminum loading exerted a pronounced nonlinear effect on the structure of pores of the hydrochar. The pristine hydrochar (prepared at 180 °C for 1 h) displayed BET surface area, pore volume and average pore diameter of 77.52 $m^2 \cdot g^{-1}$, 0.29 $cm^3 \cdot g^{-1}$, 15.15 nm, respectively, which were characteristic of a mesoporous-macroporous hybrid structure typically found in hydrochars produced under low-to-moderate hydrothermal temperatures. With the introduction of 10% $AlCl_3$, the BET surface area unexpectedly decreased to 66.73 $m^2 \cdot g^{-1}$ (a 14% reduction), while the volume of pores increased to 0.37 $cm^3 \cdot g^{-1}$. Meanwhile, the average pore diameter expanded to 22.11 nm. This may be due to insufficient catalytic activity at low concentrations of aluminum and possible blockade of pores by aluminum salts. When the $AlCl_3$ loading was increased to 30%, the structure of pores underwent significant optimization. The BET surface area surged to 111.54 $m^2 \cdot g^{-1}$ (representing an increase of 43.9%), while the pore volume increased to 0.39 $cm^3 \cdot g^{-1}$ (an increase of 34.5%). Moreover, the average pore diameter slightly decreased to 14.02 nm. This suggested that an appropriate amount of Al^{3+}, acting through the Lewis acid mechanism, catalyzed the dehydration reactions, promoted the formation of micropores, and enhanced the surface structure and pore distribution in the hydrochar, thereby increasing both the surface area and the volume of pores. This phenomenon was consistent with that reported in some previous studies [35]. Conversely speaking, increasing the dosage of aluminum to 50% diminished the BET surface area to 92.98 $m^2 \cdot g^{-1}$, the pore volume to 0.35 $cm^3 \cdot g^{-1}$ (10.3% drop relative to 30% loading of $AlCl_3$), and pore diameter to 15.24 nm, suggesting that surplus aluminum promoted the aggregation of salts, impeding access to and connectivity to the pores. This indicated that excessive aluminum loading may cause agglomeration of aluminum salts, leading to the blockade of pores and reduced pore connectivity. With the increase in hydrothermal temperature, the BET surface area of aluminum-loaded hydrochar decreased by 20% and 30% compared to the hydrochar produced at 180 °C. Nonetheless, at equivalent conditions, these modified variants invariably surpassed unmodified hydrochars in both surface area and pore volume. Therefore, aluminum loading effectively improved the porous structure of hydrochar, thereby enhancing its physisorption capacity and increasing its fluoride adsorption performance [20].

The effects of the loading of aluminum and the hydrothermal temperature on the surface morphology of sludge-derived hydrochar are illustrated in Fig. 5. The pristine hydrochar exhibited a rough surface (Fig. 5(a)–(c)) with irregularly distributed pores and microcracks (1–2 μm in width), which resulted from the shrinkage of carbonized organic matter. The addition of aluminum salt significantly modified the microstructure, yielding smaller particles and more uniform distribution of pores. This may be attributed to Al^{3+} acting as a Lewis acid catalyst to promote dehydration and decarboxylation reactions, which accelerated the decomposition of organic matter and shortened the aromatization time [35].

At the hydrothermal temperature of 180 °C, 30% $AlCl_3$ loading facilitated the hydrolysis of sludge (Fig. 5(d)), resulting in a highly porous, coral-shaped surface morphology with significantly refined distribution of pores. As the hydrothermal temperature increased, numerous AlOOH nanosheets were generated and deposited on the surface of hydrochar at 220 °C (Fig. 5(e)) [36,37]. At the hydrothermal temperature of 260 °C (Fig. 5(f)), the surface of hydrochar exhibited a layered stacking structure, with AlOOH nanosheets further thickening and partially dehydrating to form alumina. When the hydrothermal temperature exceeded 220 °C, pronounced clusters appeared on the surface of hydrochar, leading to the overlapping of active sites and hindrance to full contact with F^- during fluoride adsorption [38]. As shown in Fig. 5(g), after the adsorption of

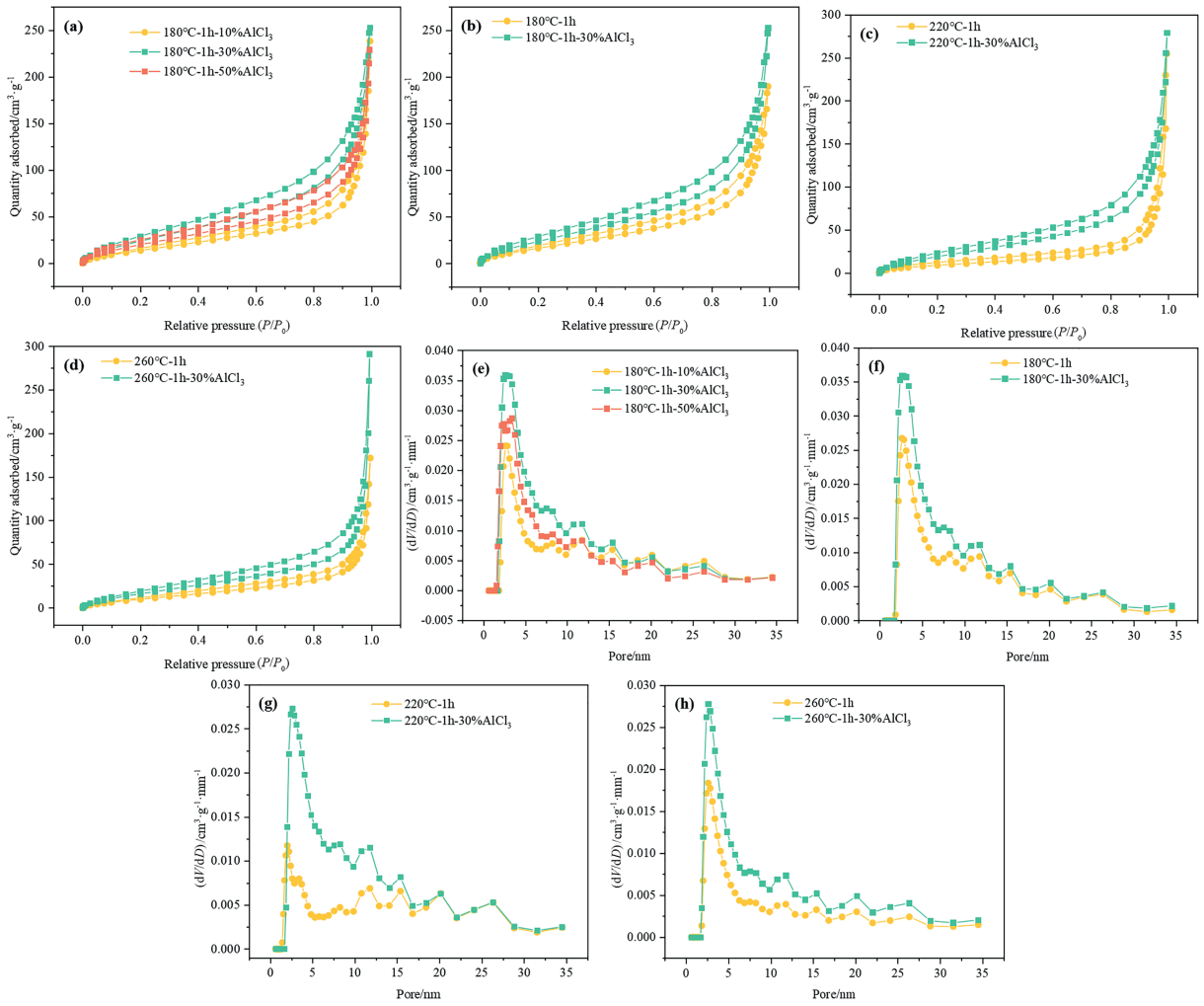


Fig. 4. N_2 adsorption/desorption isotherms (a–d) and pore size distribution curves (e–h) for aluminum-loaded hydrochar.

fluoride, the surface of hydrochar became rougher and more microspheres were formed. SEM-EDS mapping (Fig. S1(a)–(d)) revealed that the aluminum content on the hydrochar surface increased from 8.1% (mass) for the unmodified 180 °C-1 h hydrochar to 12.3% (mass) for 180 °C-1 h-30%$AlCl_3$, and further to 16.4% (mass) for 220 °C-1 h-30%$AlCl_3$, indicating successful Al loading and additional enrichment at elevated hydrothermal temperature. In contrast, the 180 °C-1 h-50%$AlCl_3$ sample exhibited a lower EDS Al content (11.7% (mass)) than the 180°C-1h-30% material, implying that raising the nominal $AlCl_3$ dosage beyond 30% did not continue to increase the accessible surface aluminum proportion. When combined with XPS, which showed a shift toward higher AlOOH/Al_2O_3 fractions at higher temperatures and loadings, and SEM observations of thicker surface coatings and partial pore coverage, these EDS results suggest that over-deposition of Al(hydr)oxides leads to agglomeration and pore blocking, enriching the overall Al signal but reducing the accessibility of reactive Al—OH sites. This integrated EDS-SEM-XPS analysis explains why the 180 °C-1 h-30%$AlCl_3$ hydrochar achieves the highest fluoride adsorption capacity, whereas samples with higher apparent surface Al exhibit diminished performance due to a larger fraction of buried or less accessible adsorption sites Furthermore, EDS mapping also confirmed the effective adsorption of fluoride (Fig. S1(e)). Additionally, XRD analysis revealed the absence of crystalline aluminum phases on the surface of synthesized aluminum-loaded hydrochar (Fig. S2), indicating that the aluminum species were predominantly amorphous [39].

Table 4
BET analysis of aluminum-loaded hydrochar.

Sample	BET/$m^2 \cdot g^{-1}$	Pore volume/ $cm^3 \cdot g^{-1}$	Average pore size/ nm
180°C-1h	77.52	0.29	15.15
220°C-1h	36.75	0.39	42.91
260°C-1h	48.77	0.27	21.79
180°C-1h-30%$AlCl_3$	111.54	0.39	14.02
220°C-1h-30%$AlCl_3$	88.88	0.43	19.43
260°C-1h-30%$AlCl_3$	77.92	0.45	23.12
180°C-1h-10%$AlCl_3$	66.73	0.37	22.11
180°C-1h-50%$AlCl_3$	92.98	0.35	15.24

3.2. Adsorption of fluoride

The present study investigated the adsorption of fluoride using aluminum-loaded hydrochar by systematically evaluating the effect of key operating parameters (pH, dosage, and contact time) on

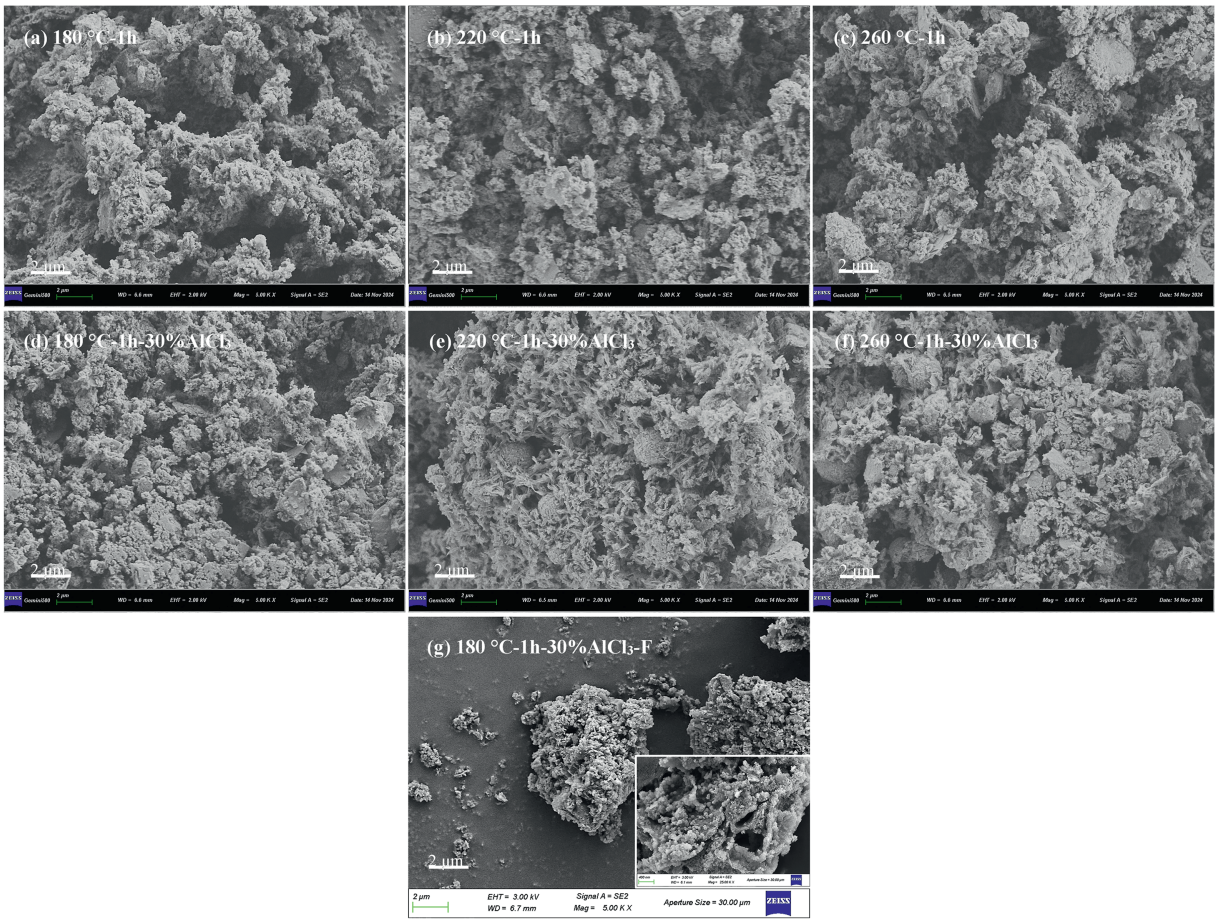


Fig. 5. SEM of aluminum-loaded hydrochar.

adsorption, adsorption kinetics, thermodynamic properties of the adsorbent, effects of coexisting anions, and recyclability of the adsorbent, thus providing theoretical foundations for practical applications to real-world wastewater.

3.2.1. Effect of the dosage of adsorbent and pH value

Fluoride sorption onto hydrochar was markedly influenced by the adsorbent dosage, as depicted in Fig. 6(a). Increasing the adsorbent's dosage from 0.1 to 0.125 g increased the adsorption capacity from 5.07 to 9.87 $mg \cdot g^{-1}$. With further increase in the dosage of adsorbent, the adsorption capacity progressively decreased. This variation trend occurred because lower dosages made more adsorption sites available, significantly enhancing the adsorption of fluoride [40]. However, higher dosages caused the aggregation of particles through either van der Waals forces or electrostatic attraction, reducing the effective surface area. Excess adsorbent also led to underutilized adsorption sites, decreasing the adsorption capacity [41].

The pH of the solution also played a pivotal role in sorption dynamics, as shown in Fig. Fig. 6(b). Hydrochar maintained high fluoride removal efficiency across the pH range of 2–11. At low pH (2–3), protonation of surface functional groups imparts a positive charge, enhancing the electrostatic attraction with F^- and improving the adsorption capacity [42]. However, when pH was less than 3, partial conversion of F^- to HF (pK_a of 3.17) reduced the adsorption efficiency due to hydrophobic interactions and low polarity [43]. In the pH range of 4–5, weakened surface charge diminished the electrostatic attraction, lowering the adsorption capacity [44]. At the pH of 6, diminished electrostatic forces were compensated by ion exchange ($\equiv Al—OH + F^- \rightarrow \equiv Al—F + OH^-$) [41]. Additionally, protonated —OH groups ($\equiv Al—OH_2^+$) participated in ligand exchange with F^-, achieving the highest adsorption capacity (13.93 $mg \cdot g^{-1}$) observed in the present study [45]. In line with zeta potential measurements conducted *via* the pH drift method (Fig. S3), the hydrochar displayed a point of zero charge (pH_{pzc}) of 6.52, rendering the surface near-neutral or slightly positive at pH ~ 6 and thereby minimizing electrostatic repulsion to facilitate F^- access to Al—OH sites through enhanced electrostatic attraction and complexation. At pH ~ 7, the zeta potential became negative ($\zeta = -22.63$ mV), introducing partial repulsion against the anionic fluoride species; nonetheless, defluorination persisted *via* site-specific ligand exchange on aluminum functional groups, though with somewhat diminished effectiveness relative to pH 6.0. Increasing the pH range to 7–8 triggered a sharp decline in adsorption capacity, as increasing OH^- concentrathions neutralized the surface charge, abolishing the electrostatic pull, while OH^- and F^- vied for the active sites due to analogous charges and sizes [46]. Interestingly, for the pH range of 9–10, the adsorption capacity gradually increased from 9.42 $mg \cdot g^{-1}$ to 12.84 $mg \cdot g^{-1}$, possibly due to the formation of hydroxyl complexes such as $Al(OH)_4^-$ on the surface of hydrochar, these complexes could adsorb F^- through complexation reactions. Beyond this, increased negative surface charge fostered F^- repulsion, compounded by OH^- dominance, thus curtailing the sorption of F^- [20].

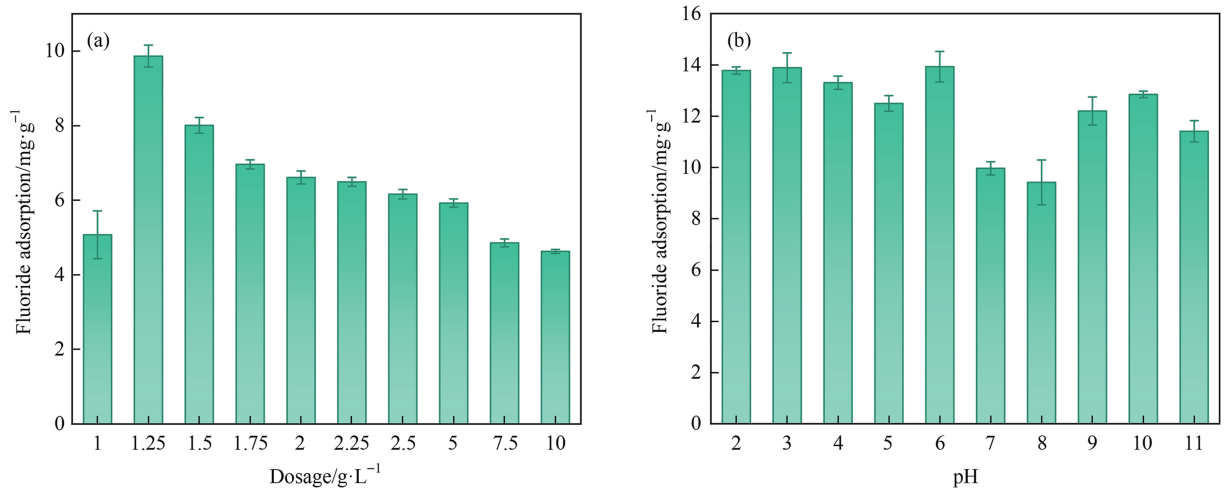


Fig. 6. Effect of adsorbent dosage (a) and pH value (b) on the adsorption of fluoride using aluminum-loaded hydrochar at 180°C-1h-30%-$AlCl_3$.

3.2.2. *Adsorption kinetics*

Adsorption kinetics for fluoride's uptake by hydrochar were evaluated using pseudo-first-order, pseudo-second-order, and intraparticle diffusion models. The resulting profiles are presented in Fig. 7, with fitted parameters detailed in Table 5. The pseudo-second-order model yielded an excellent correlation (R^2 = 0.97, Fig. 7(b)), outperforming the pseudo-first-order model (Fig. 7(a)) and implying that chemisorption primarily governed the

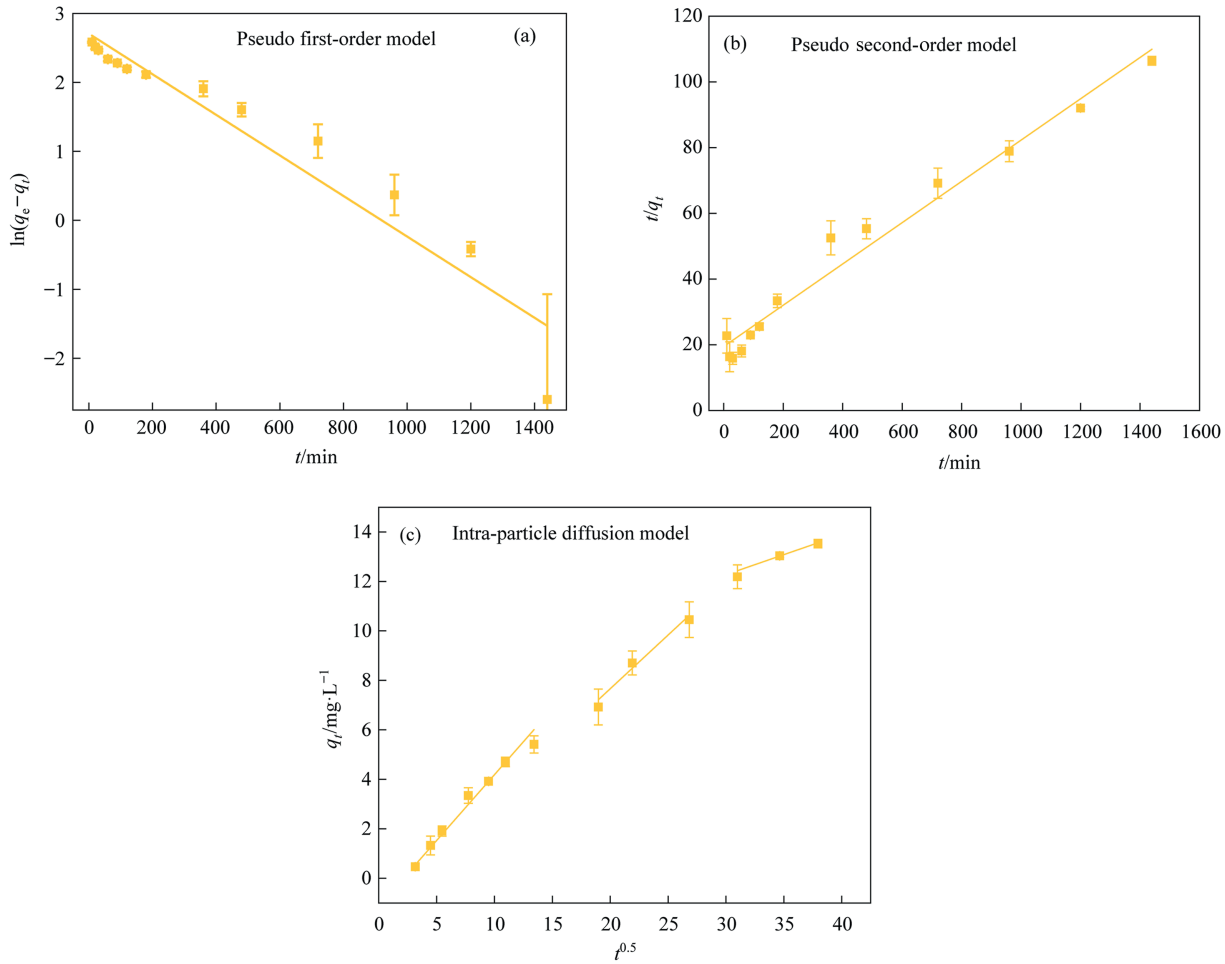


Fig. 7. Linear graph of pseudo first-order model (a), pseudo second-order model (b), and intra-particle diffusion model (c) for aluminum-loaded hydrochar at 180 °C-1 h-30%-$AlCl_3$.

Table 5
Kinetic parameters for the adsorption of fluoride ions on the adsorbent.

Model	Parameter 1	Parameter 2	R^2
Pseudo first-order	k_1=(6.77 ± 0.60) × 10^{-3} min^{-1}	q_{e1}=(14.98 ± 2.51) $mg·g^{-1}$	0.91
Pseudo second-order	k_2=(2.03 ± 0.28) × 10^{-4} min^{-1}	q_{e2}=(15.92 ± 0.75) $mg·g^{-1}$	0.97
Intra-particle diffusion	K_1=(0.53 ± 0.017) $mg·(g·h^{0.5})^{-1}$	C_1 = −1.14 ± 0.16	0.99
	K_2=(0.43 ± 0.082) $mg·(g·h^{0.5})^{-1}$	C_2 = −1.02 ± 1.85	0.93
	K_3=(0.16 ± 0.028) $mg·(g·h^{0.5})^{-1}$	C_3 = 7.42 ± 1.00	0.94

adsorption process [38]. Furthermore, as shown in Fig. 7(c), the intraparticle diffusion model exhibited a classic three-stage characteristic, as outlined below.

Stage I: Liquid film diffusion dominated the process with the rate constant (K_1) of 0.53 ± 0.017 $mg·(g·h^{0.5})^{-1}$, indicating F^- overcame the boundary layer resistance to reach the surface of particles. This stage contributed around 40% of the total adsorption.
Stage II: Intraparticle diffusion became rate-limiting step, with a rate constant (K_2) of 0.43 ± 0.082 $mg·(g·h^{0.5})^{-1}$, showing a 19% decrease in the adsorption capacity compared to the adsorption capacity observed in Stage I, which was due to increased diffusion resistance within mesopores.
Stage III: The rate constant (K_3) of 0.16 ± 0.028 $mg·(g·h^{0.5})^{-1}$ approached zero, confirming that active sites were nearly saturated and the dynamic equilibrium was achieved.

The non-zero intercept ($C \neq 0$) in the fitted line underscored the combined influence of boundary layer effects and surface reactions in conjunction with intraparticle transport, which was consistent with chemisorption as the rate-limiting factor per the pseudo-second-order framework [47].

3.2.3. Adsorption isotherm

Fluoride sorption isotherms for hydrochar (synthesized at 180 °C for 1 h with 30% $AlCl_3$) were determined at 25 °C, 35 °C, and 45 °C, as illustrated in Fig. 8. The isotherm data were fitted using both the Langmuir and Freundlich models, with the corresponding fitting parameters summarized in Table 6. Elevated temperatures incrementally boosted the sorption capacity, signifying an endothermic process in which thermal energy promoted the uptake of fluoride, though the temperature sensitivity remained modest. The Langmuir model projected a saturation capacity of 24.10 $mg·g^{-1}$, representing a 9.86-fold improvement over unmodified hydrochar and highlighting the efficacy of aluminum functionalization in augmenting defluoridation. Across all temperatures, the Freundlich model achieved superior correlations ($R^2 > 0.98$) relative to Langmuir, implying multilayer sorption on a non-homogeneous surface, which was consistent with the variable porosity of the prepared hydrochar. The larger Langmuir constant (K_L) and the lower Freundlich constant ($1/n$) indicated that aluminum-loaded hydrochar is not only advantageous but also effective throughout the fluoride ion adsorption process [48,49].

For objective evaluation of the defluoridation performance of aluminum-loaded hydrochar, Table 7 compares maximum capacities of various aluminum-modified adsorbents for fluoride. Our hydrochar excels in cost-effectiveness, with production costs below 0.5 $USD·kg^{-1}$ from sewage sludge waste (using free sludge feedstock and minimal chemicals). It's 70% to 80% cheaper than aluminum-modified natural zeolite (1.50–2.50 $USD·kg^{-1}$, due to zeolite synthesis, Al grafting and energy-intensive calcination). It aligns with existing municipal sludge infrastructure, with integrated heat recovery facilities handling 10–50 $t·d^{-1}$ surpassing aluminum-modified hydroxyapatite (which requires precise layered co-precipitation and faces large-batch uniformity issues from precursor constraints). Though its maximum adsorption capacity is slightly lower than some lab-optimized materials, it outperforms most multi-step aluminum-modified adsorbents in practical applications.

3.2.4. Effect of competing anions

Fluoride-containing wastewater often harbors diverse anions that vie for binding sites on adsorbents. Therefore, assessing the impact of these coexisting species on the defluoridation efficacy of aluminum-functionalized hydrochar is essential. Fig. 9 delineates the influence of competing anions at varying levels (50, 100, and 150 $mg·L^{-1}$) on fluoride sequestration. The order of interference in descending order was found to be: SO_4^{2-} >NO_3^- >PO_4^{3-} >Cl^-. This may be attributed to the higher charge-to-radius ratio (Z/r) of SO_4^{2-} (SO_4^{2-} (2/0.230) > F^- (1/0.133)), as well as its ability to react with polymeric aluminum species and Al—F complexes on the surface of hydrochar to form co-precipitates of Al-SO_4, thereby releasing F^- and severely hindering the removal of fluoride [45,53,54].

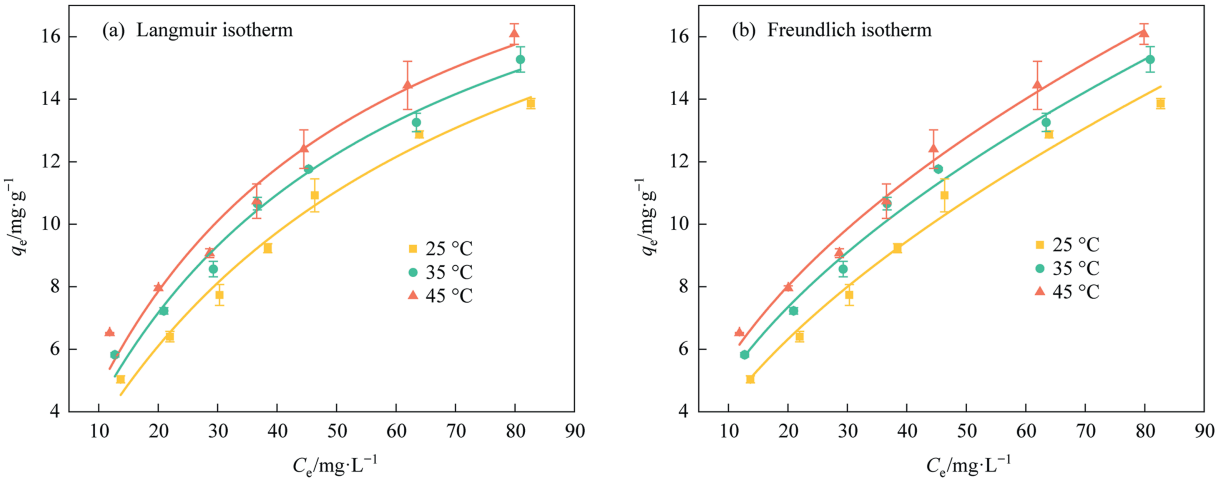


Fig. 8. Non-linear fits of Langmuir isotherm (a), and Freundlich isotherm (b) at 25 °C, 35 °C, and 45 °C for aluminum-loaded hydrochar at 180 °C-1 h-30%-$AlCl_3$.

Table 6
Isotherm parameters of Langmuir and Freundlich models for the adsorption of fluoride by adsorbent.

T/°C	Langmuir isotherm			Freundlich isotherm		
	K_L/L·g^{-1}	q_{max}/mg·g^{-1}	R^2	K_F/mg·g^{-1}	1/n	R^2
25	0.017 ± 0.0024	24.10 ± 1.86	0.98	1.11 ± 0.16	0.58 ± 0.037	0.98
35	0.022 ± 0.0033	23.24 ± 1.69	0.98	1.51 ± 0.17	0.53 ± 0.028	0.99
45	0.025 ± 0.0048	23.70 ± 0.19	0.96	1.75 ± 0.16	0.51 ± 0.024	0.99

Moreover, as the concentration of competing anions increased, their inhibitory effects became more pronounced, leading to a progressive decrease in the defluoridation efficiency of aluminum-loaded hydrochar.

Nevertheless, the inhibitory effects of all anions on the removal of fluoride by aluminum-loaded hydrochar were limited. This is because anions with larger ionic radii and higher charges only partially influenced charge repulsion and steric hindrance, and could only partially displace fluoride ions from the adsorption sites [45].

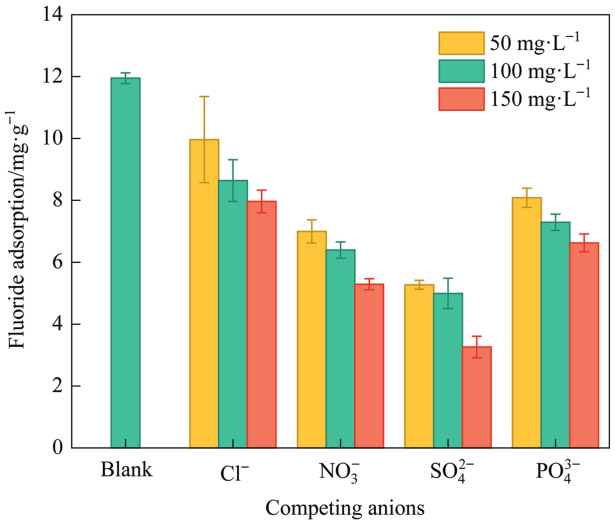


Fig. 9. Effects of different concentrations of coexisting anions on the removal of fluoride using aluminum-loaded hydrochar.

3.2.5. Reuse of adsorbent and application to industrial effluent sample

The feasibility of regenerating aluminum-loaded hydrochar was investigated by immersing the spent adsorbent in 0.5 mol·L^{-1} Na_2CO_3 solution followed by drying. Five consecutive adsorption-desorption cycles were conducted under identical experimental conditions to evaluate the stability and reusability of the adsorbent. As illustrated in Fig. 10(c), after the fifth cycle, the adsorption capacity remained at 70.04% of the initial value, indicating that the adsorbent possessed good stability and excellent regeneration performance [34]. Beyond monitoring fluoride removal across repeated cycles, the structural stability of the 180 °C-1 h-30% $AlCl_3$ hydrochar was assessed *via* SEM-EDS and N_2 adsorption before and after five regeneration cycles. SEM images (Fig. 10(a)) demonstrated that the regenerated adsorbent maintained its granular, porous structure without obvious particle collapse or fragmentation. In contrast, N_2 sorption analysis (Fig. 10(d)–(e)) revealed a substantial decrease in BET surface area to 34.17 m^2·g^{-1}, alongside a total pore volume of 0.17 cm^3·g^{-1} and an average pore diameter of 19.94 nm. Notably, the pore diameter distribution shifted from a mesopore-dominant to a macropore-prevalent profile, which could be attributed to the corrosion induced by the alkaline regeneration solution. EDS analysis (Fig. 10(b)), however, showed a negligible change in aluminum content relative to the fresh material, confirming limited Al leaching and robust Al immobilization. Fig. S4 reveals that the hydroxyl density of

Table 7
Defluoridation performance of different aluminum-modified adsorbents.

Adsorbent	Preparation conditions	Adsorption conditions	Measured fluoride adsorption capacity/mg·g^{-1}	Ref.
Aluminum-hydroxide-modified diatomite	Impregnation with 1 mol·L^{-1} $AlCl_3·6H_2O$, 3 mol·L^{-1} NaOH, 2 h	0.1 g adsorbent, 120 min, 25 ml, 100 mg·L^{-1} F$^-$, pH 4	24.80	[41]
Aluminum-modified hydroxyapatite	Co-precipitation: $Ca(NO_3)_2$ and $Al(NO_3)_3$, Al/Ca = 0–0.5, pH 9, 100 °C, 6 h aging, dried at 70 °C overnight	0.05 g adsorbent, 120 min, 100 ml, 100 mg·L^{-1} F$^-$, pH 7, 25 °C	32.57	[50]
Aluminum modified activated carbon	Impregnation of AC with 0.13 mol·L^{-1} $Al(NO_3)_3$, pH neutralized, dried at 105 °C	4 g·L^{-1} adsorbent, 15 min, 100 ml, 10–250 mg·L^{-1} F$^-$, pH 7	20.40	[40]
Aluminum and bone carbon loaded polyurethane foam	$AlCl_3$ (1.2 g) and phthalic acid (3.2 g) dissolved in 150 ml deionized water, stirred 3 h at room temperature, then poured into the reactor containing the polyurethane foam, heated at 100 °C for 24 h; added chicken bone biochar (1 g, calcined at 600 °C for 2 h) dispersed in 150 ml water and heated at 100 °C for 24 h; dried to obtain composite	0.1 g adsorbent, 120 min, 50 ml, 20 mg·L^{-1} F$^-$, pH 5.5, 25 °C	7.96	[45]
Aluminum-modified natural zeolite	Impregnation with 15% (mass) $Al_2(SO_4)_3·18H_2O$, 6h	1.0 g adsorbent, 300 min, 100 ml, 10–80 mg·L^{-1} F$^-$, pH 6, 25 °C	0.98	[43]
Aluminum hydroxide coated zeolite (AHZ)	AHZ *via* coal fly ash-NaOH hydrothermal treatment, $AlCl_3$ neutralization	0.1 g adsorbent, 24 h, 100 ml, 5–200 mg·L^{-1} F$^-$, pH 6, 25 °C	18.12	[51]
Al/La modified acidified attapulgite composite materials	Natural attapulgite: Crushed to 6 mm, ball-milled, 200-mesh (127 μm) sieved, dried, 15% H_2SO_4 treated (72 h, 180 r·min^{-1}, 25 °C, oscillated).	0.05 g adsorbent, 24 h, 100 ml, 1–500 mg·L^{-1} F$^-$, 25 °C	130.42	[52]
Aluminum-loaded sludge hydrochar	Hydrothermal with $AlCl_3·6H_2O$, 180 °C, 1 h, 30% Al	0.1 g adsorbent, 24 h, 50 ml, 20–100 mg·L^{-1} F$^-$, pH 6, 25 °C	16.08	This study

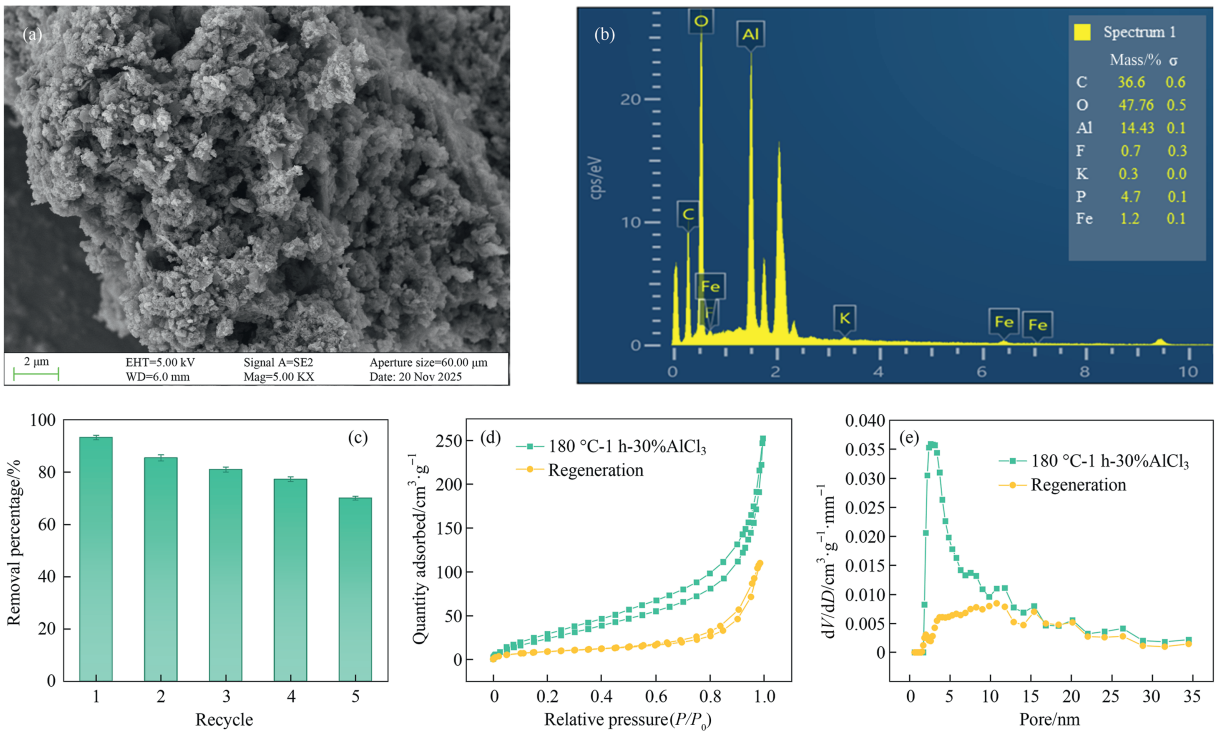


Fig. 10. Characterization and regeneration performance of aluminum-loaded hydrochar adsorbent: SEM-EDS (a-b), fluoride removal efficiency over cycles (c), and N_2 adsorption-desorption analysis (d-e).

the adsorbent partially recovered after regeneration but still remains lower than that of the sample before fluoride adsorption. These results indicated that the gradual decline in fluoride removal efficiency during cycling stems primarily from partial pore blockage, and the aforementioned structural shift due to corrosion, rather than severe degradation of the hydrochar matrix or extensive Al loss.

Practical utility for defluoridation was further validated using authentic wastewater sourced from a facility in Dongzhi County (China), featuring 821.61 mg·L^{-1} NO_3^- and 1446.49 mg·L^{-1} SO_4^{2-} as well as an initial F^- concentration of 6.68 mg·L^{-1}. After adding 0.125 g of hydrochar and conducting adsorption for 2 h, the concentration of fluoride was reduced to 2.71 mg·L^{-1}. This result was similar to the adsorption isotherm data obtained at low concentrations (2–10 mg·L^{-1}), where the adsorption capacity was 3.39 mg·g^{-1}. These results demonstrated that, despite the presence of coexisting ions in actual wastewater, aluminum-loaded hydrochar exhibited outstanding defluoridation performance. While the Al-modified hydrochar demonstrates superior defluorination performance, potential environmental risks associated with aluminum release during adsorption must be considered to ensure safe application in wastewater treatment. Leaching experiments were performed by adding 0.1 g of aluminum-loaded hydrochar to 100 ml deionized water, shaking the mixture for 2 h, and analyzing the filtered solution *via* ICP-OES, which revealed an aluminum concentration of 1.24 mg·L^{-1}. This value was substantially below industrial discharge limits (<5 mg·L^{-1} for non-potable effluents) and posed low risk of secondary pollution, though enhanced leaching might occur in acidic conditions and large-scale use; mitigation *via* pH control and effluent polishing was thus considered. Therefore, aluminum-loaded hydrochar emerges as a viable candidate for remediating fluoride-laden industrial discharges.

3.3. Aluminum precursor control and adsorption mechanism of aluminum-loaded hydrochar

As shown in Fig. 11, the regulation mechanism of aluminum precursor types on the physicochemical properties of hydrochar and the fluoride adsorption mechanism of the derived aluminum-loaded hydrochar are illustrated. The precursor-dependent hydrolysis and speciation of aluminum directly governed the physicochemical properties of the sludge-derived hydrochar. Chloride ions facilitated moderate hydrolysis and the balanced formation of $Al(OH)_3$ and AlOOH, whereas sulfate ions exerted strong templating effects, causing ordered layered structures with enhanced porosity. Meanwhile, nitrate ions accelerated the hydrolysis process and favored the formation of alumina. These transformations enriched the surface hydroxyl functionalities and promoted the dehydration and aromatization of organic matter, thus contributing to hierarchical porous networks with elevated surface areas and pore volumes that synergistically enhanced the adsorption of fluoride.

The defluoridation process of aluminum-loaded hydrochar involves multiple synergistic mechanisms. XPS analysis revealed that the aluminum species loaded onto the hydrochar were primarily present as $Al(OH)_3$ and AlOOH. These aluminum hydroxide components played a central role during adsorption, providing various active sites for the removal of fluoride. The hydrochar substrate contributed a substantial surface area and intricate porosity, while its inherent functional moieties were engaged in sorption, yielding an integrated system with enhanced efficacy.

The large surface area and hierarchical porous structure of hydrochar enabled the adsorption of F^- through pore filling. This mechanism mainly relies on the physical properties of the material and is classified as physisorption. Both SEM and BET analyses indicated that the loading of aluminum led to the formation of a more complex, layered porous structure, retaining the original

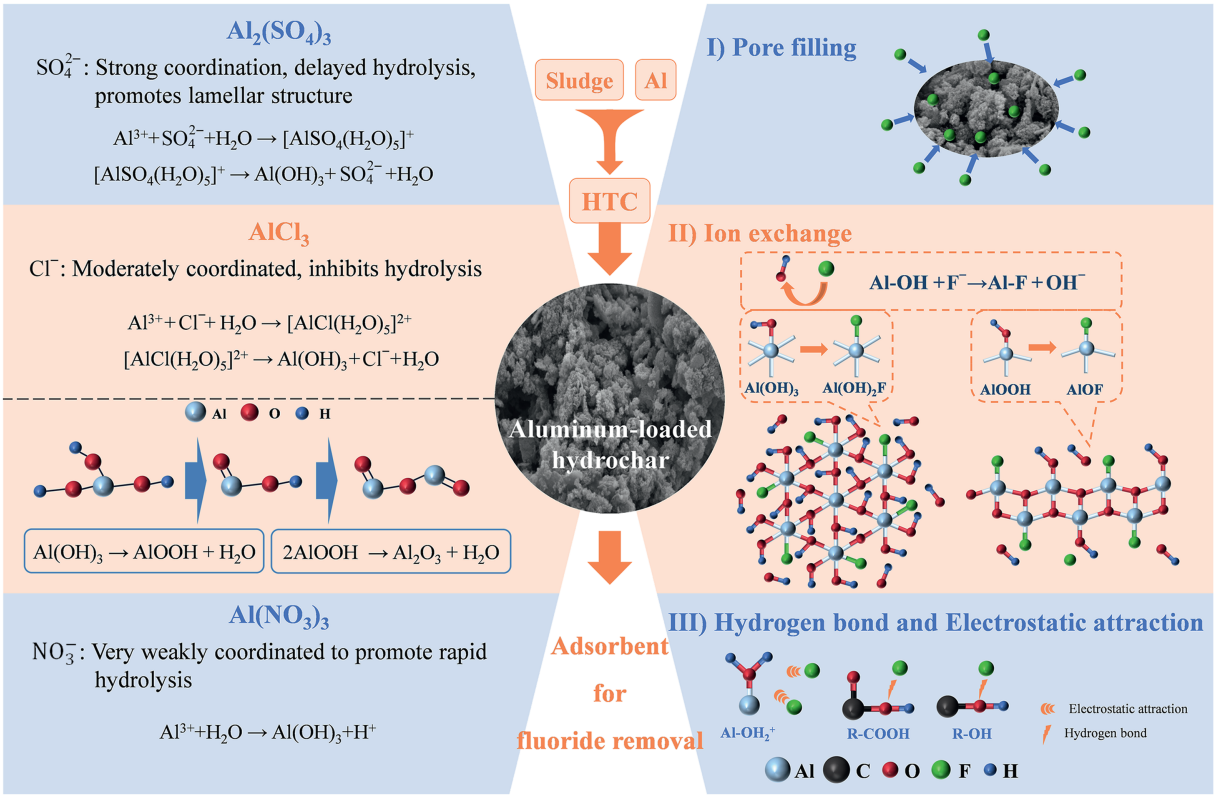


Fig. 11. Mechanism of fluoride's removal by aluminum-loaded hydrochar.

macropores while generating abundant mesopores and micropores on the surface. These pores of various sizes provided favorable pathways for the diffusion and adsorption of fluoride ions. Under mildly acidic conditions (pH range of 4–6), the surface of aluminum hydroxides became protonated to form Al—OH^{2+}, which adsorbed F^- through electrostatic attraction. Meanwhile, oxygen-containing functional groups such as carboxyl and hydroxyl groups on the carbon matrix formed hydrogen-bonding networks with F^-, resulting in a combination of physical and chemical adsorption. The core chemical mechanism was attributed to hydroxyl-fluoride ion exchange.

4. Conclusions

In the present study, a series of aluminum-loaded hydrochar adsorbents were successfully synthesized through a co-hydrothermal reaction using sewage sludge and various aluminum precursors ($AlCl_3$, $Al_2(SO_4)_3$, $Al(NO_3)_3$, $Al(OH)_3$, and Al_2O_3). The defluoridation performance of aluminum-loaded hydrochar prepared using $AlCl_3$ was systematically investigated. Combined XPS and XRD analyses revealed that the coordination ability of anions in the aluminum precursors significantly influenced the speciation of active aluminum species. For instance, in the $AlCl_3$ system, Cl^- formed $[AlCl(H_2O)_5]^{2+}$ complexes with Al^{3+}, which retarded the hydrolysis kinetics and promoted the synergistic formation of $Al(OH)_3$ (39.04%) and AlOOH (47.52%). In the $Al_2(SO_4)_3$ system, SO_4^{2-} strongly coordinated with Al^{3+}, suppressing the initial hydrolysis and guiding the oriented growth of layered hydroxides, thus resulting in significant enrichment of $Al(OH)_3$ (44.29%) and AlOOH (52.72%). In contrast, the weak coordination in the $Al(NO_3)_3$ system led to dehydroxylation of hydrolysis products and the formation of 20.92% Al_2O_3, whereas the $Al(OH)_3$ system yielded AlOOH (29.85%) and Al_2O_3 (48.53%) through surface reconstruction. The inertness of Al_2O_3 resulted in 49.73% unconverted phase, confirming that the $AlCl_3$ system was the most favorable for stabilizing active aluminum species. Furthermore, XRD results indicated that aluminum was loaded onto the hydrochar in an amorphous form.

Incorporating 30% $AlCl_3$ enabled Al^{3+} to function as a Lewis acid, facilitating dehydration and decarboxylation pathways that accelerated the degradation of organic matter and fostered the evolution of micro- and meso-pores, consequently escalating the BET surface area from 77.52 $m^2 \cdot g^{-1}$ to 111.54 $m^2 \cdot g^{-1}$ of the unmodified hydrochar. Kinetic evaluations confirmed chemisorption as the prevailing mechanism, which aligned well with the pseudo-second-order model, while isothermal data favored the Freundlich model over the Langmuir model, signifying heterogeneous multilayer binding with a projected saturation uptake of 24.10 $mg \cdot g^{-1}$, with primary adsorption pathways encompassing ion exchange, electrostatic attraction, and pore filling. Additionally, aluminum-loaded hydrochar exhibited excellent regeneration performance, retaining 70.04% of its adsorption capacity after five cycles. Furthermore, the existence of co-occurring anions impeded the binding of fluoride to the adsorbent in the descending order of: $SO_4^{2-} > NO_3^- > PO_4^{3-} > Cl^-$. Overall, these results demonstrated that aluminum-loaded hydrochar could effectively remove low concentrations of fluoride from real wastewater and possessed outstanding reusability.

CRediT Authorship Contribution Statement

Fuqiang Xu: Writing – original draft, Visualization, Investigation, Data curation. Miao Gong: Writing – review & editing, Writing – original draft, Supervision, Funding acquisition,

Conceptualization. Piao Liu: Writing – original draft, Visualization. Qiao Xu: Visualization, Resources. Ying Su: Writing – review & editing, Methodology. Yujie Fan: Writing – review & editing, Resources. Shuai Guo: Writing – review & editing, Resources.

Declaration of Competing Interest

The authors declare that they have no known competing financial interests or personal relationships that could have appeared to influence the work reported in this paper.

Acknowledgements

The authors are grateful for the financial support from the Natural Science Foundation of Anhui Province (2408085ME118), the National Natural Science Foundation of China (52000056), and the Fundamental Research Funds for the Central Universities (JZ2021HGTB0104).

Supplementary Material

Supplementary data to this article can be found online at https://doi.org/10.1016/j.cjche.2025.12.047.

References

[1] H.M. Chang, Y. Zhao, V. Bisinella, A. Damgaard, T.H. Christensen, Climate change impacts of conventional sewage sludge treatment and disposal, *Water Res.* 240 (2023) 120109.
[2] S.J. Ma, C.B. Zhou, J.J. Pan, G. Yang, C.L. Sun, Y.J. Liu, X.C. Chen, Z.L. Zhao, Leachate from municipal solid waste landfills in a global perspective: characteristics, influential factors and environmental risks, *J. Clean. Prod.* 333 (2022) 130234.
[3] H. Xia, J. Tang, L. Aljerf, T.Z. Wang, B.Y. Gao, Q.D. Xu, Q. Wang, P. Ukaogo, Assessment of PCDD/Fs formation and emission characteristics at a municipal solid waste incinerator for one year, *Sci. Total Environ.* 883 (2023) 163705.
[4] Y.F. Xu, L. Zhu, S.G. Chen, H.Y. Wu, R.Q. Li, J. Li, J. Yuan, T. Wen, C. Xue, Q.R. Shen, Risk assessment and dissemination mechanism of antibiotic resistance genes in compost, *Bioresour. Technol.* 378 (2023) 129656.
[5] M. Gong, F.Q. Xu, P. Liu, Q. Xu, Y. Su, Y.J. Fan, M.D. Li, A review of biomass hydrochar as an adsorbent: performance, modification, and applications, *J. Water Process Eng.* 71 (2025) 107314.
[6] W.T. Chen, M.A. Haque, T.F. Lu, A. Aierzhati, G. Reimonn, A perspective on hydrothermal processing of sewage sludge, *Curr. Opin. Environ. Sci. Health* 14 (2020) 63–73.
[7] R. Ferrentino, R. Ceccato, V. Marchetti, G. Andreottola, L. Fiori, Sewage sludge hydrochar: an option for removal of methylene blue from wastewater, *Appl. Sci.* 10 (10) (2020) 3445.
[8] L.Y. Chen, D.P. Li, Y. Huang, W.J. Zhu, Y.Q. Ding, C.R. Guo, Preparation of sludge-based hydrochar at different temperatures and adsorption of BPA, *Water Sci. Technol.* 82 (2) (2020) 255–265.
[9] N. Musa, B.K. Allam, N.B. Singh, S. Banerjee, Investigation on water defluoridation *via* batch and continuous mode using Ce-Al bimetallic oxide: adsorption dynamics, electrochemical and LCA analysis, *Environ. Pollut.* 328 (2023) 121639.
[10] A. Mukherjee, A. Chowdhury, M.K. Adak, J. Khatun, P. Dhak, D. Dhak, Fluoride adsorption and photoreduction of Cr(VI) using heterogeneous Al^{3+} modified mine-waste, an *in-situ* approach, *J. Environ. Chem. Eng.* 8 (3) (2020) 103759.
[11] M. Qasemi, M. Farhang, M. Morovati, M. Mahmoudi, S. Ebrahimi, A. Abedi, J. Bagheri, A. Zarei, J. Bazeli, M. Afsharnia, S. Ghalehaskar, A. Ghaderpoury, Investigation of potential human health risks from fluoride and nitrate *via* water consumption in Sabzevar, Iran, *Int. J. Environ. Anal. Chem.* 102 (2) (2022) 307–318.
[12] S.J.E., K.V. Sarath, M. Santosh, P.K. Krishnaprasad, B.K. Arya, M.S. Babu, Fluoride contamination in groundwater: a global review of the status, processes, challenges, and remedial measures, *Geosci. Front.* 15 (2) (2024) 101734.
[13] Y.M. Jiang, C.Q. Li, X.L. Huang, B.C. Hao, X.T. Li, J. Ma, H. Mao, S.L. Zhao, Y. Liao, Zirconium loaded on tannin foam for efficient adsorptive removal of fluoride at low concentration in a wide pH range, *Desalin, Water Treat.* 250 (2022) 159–171.
[14] W.Z. Gai, S.H. Zhang, Y. Yang, X.H. Zhang, Z.Y. Deng, Separation of excess fluoride from water using amorphous and crystalline AlOOH adsorbents, *ACS Omega* 6 (25) (2021) 16488–16497.
[15] Y.P. Huang, D.K. Shen, Z.H. Wang, Preparation of citric acid-sewage sludge hydrochar and its adsorption performance for Pb(II) in aqueous solution, *Polymers* 14 (5) (2022) 968.
[16] A. Bhatnagar, E. Kumar, M. Sillanpää, Fluoride removal from water by adsorption: a review, *Chem. Eng. J.* 171 (3) (2011) 811–840.
[17] Z. He, R.P. Liu, J. Xu, H.J. Liu, J.H. Qu, Defluoridation by Al-based coagulation and adsorption: species transformation of aluminum and fluoride, *Sep. Purif. Technol.* 148 (2015) 68–75.
[18] W.T. Kim, J.W. Lee, H.E. An, S.H. Cho, S. Jeong, Efficient fluoride wastewater treatment using eco-friendly synthesized AlOOH, *Nanomaterials* 13 (21) (2023) 2838.
[19] X.Q. Zhang, Y.L. Qi, Z.H. Chen, N.N. Song, X. Li, D.J. Ren, S.Q. Zhang, Evaluation of fluoride and cadmium adsorption modification of corn stalk by aluminum trichloride, *Appl. Surf. Sci.* 543 (2021) 148727.
[20] S.S. Li, M.S. Song, L. Tong, C.Q. Ye, Y.H. Yang, Q.W. Zhou, Enhancing fluoride removal from wastewater using Al/Y amended sludge biochar, *Environ. Sci. Pollut. Res. Int.* 30 (60) (2023) 125832–125845.
[21] I. Yakub, K.A.M. Said, M.A.M. Amin, A.B.H. Kueh, M. Amran, Aqueous-phase reforming of glycerol using Cu-Ni bimetal catalyst supported over coconut shell activated carbon, *J. Adv. Res. Fluid Mech. Therm. Sci.* 115 (1) (2024) 193–205.
[22] C.S. Hou, W. Xiu, H.M. Guo, S.M. Li, C.P. Jiang, Application of Al-Fe co-modified rice-straw biochar to fluoride removal: synthesis, optimization, and performance, *Water Air Soil Pollut.* 234 (3) (2023) 169.
[23] W. Li, P.C. Xie, H.Y. Zhou, H.Y. Zhao, B. Yang, J. Xiong, Preparation of lanthanum-modified tea waste biochar and its adsorption performance on fluoride in water, *Materials* 17 (3) (2024) 766.
[24] M. Olivares-Marin, S. Román, B. Ledesma, A. Álvarez, Optimizing Al and Fe load during HTC of water hyacinth: improvement of induced HC physicochemical properties, *Catalysts* 13 (3) (2023) 506.
[25] H.K. Park, K.Y. Park, H.J. Kim, Kinetics of gas-phase hydrolysis of aluminum chloride for alumina particles, *Ind. Eng. Chem. Res.* 53 (39) (2014) 14956–14962.
[26] X. Wang, H. Xu, D.S. Wang, Mechanism of fluoride removal by $AlCl_3$ and Al_{13}: the role of aluminum speciation, *J. Hazard. Mater.* 398 (2020) 122987.
[27] F. Xiao, B.J. Zhang, C. Lee, Effects of low temperature on aluminum(III) hydrolysis: theoretical and experimental studies, *J. Environ. Sci.* 20 (8) (2008) 907–914.
[28] S.S. Singh, Hydrolytic reactions and properties of dilute aluminum salt solutions, *Can. J. Soil Sci.* 62 (4) (1982) 559–569.
[29] W.Y. Zhu, Z.L. Li, Y.H. Tan, G.X. He, X.X. Jiang, Y.B. Li, W.G. Zhang, X.L. Chen, Enhanced fluoride removal performance from water by calcined-state mayenite ($Ca_{12}Al_{14}O_{33}$): adsorption characteristics and mechanism, *Materials* 18 (10) (2025) 2189.
[30] F. Liu, Q. Zhao, Y.G. Xia, X.L. Jiao, D.R. Chen, Elucidating the hydrolysis and polymerization reactions of Al^{3+}-solvated molecules by reactive molecular dynamics simulation, *Int. J. Quant. Chem.* 124 (19) (2024) e27483.
[31] T. Yoshida, T. Yamaguchi, Y. Iida, S. Nakayama, XPS study of Pb(II) adsorption on.GAMMA.-Al_2O_3 surface at high pH conditions, *J. Nucl. Sci. Technol.* 40 (9) (2003) 672–678.
[32] A. Nylund, I. Olefjord, Surface analysis of oxidized aluminium. 1. Hydration of Al_2O_3 and decomposition of $Al(OH)_3$ in a vacuum as studied by ESCA, *Surf. Interface Anal.* 21 (5) (1994) 283–289.
[33] Z. Wang, X.Y. Gu, Y.F. Zhang, X.B. Zhang, H.H. Ngo, Y. Liu, W.B. Jiang, X.N. Tan, X. Wang, J.Q. Zhang, Activated nano-Al_2O_3 loaded on polyurethane foam as a potential carrier for fluorine removal, *J. Water Process Eng.* 44 (2021) 102444.
[34] L.B. Li, Z.H. Chen, J.H. Wang, Y.Y. Tang, K. Yang, Z. Fang, Mechanism and performance of porous inflorescence-like Al_2O_3-TiO_2 for removing fluorine ions in industrial $ZnSO_4$ solution, *J. Environ. Chem. Eng.* 13 (1) (2025) 115283.
[35] L.T. Tran, H.T. Hoang, M.Q. Nguyen, N.D. Dao, T.H.T. Vu, Effect of $FeCl_3$ catalyst on chemical properties of hydrochar produced by hydrothermal carbonization of dragon fruit stem (hylocereus undatus), *Bioenergy Res.* 15 (4) (2022) 1996–2005.
[36] K. Nahar, I.G. Hakeem, A. Surapaneni, A.S. Ball, K. Shah, Co-processing of sewage sludge with alum sludge and food and garden organics: towards boehmite generation and enhanced product properties, *J. Environ. Chem. Eng.* 13 (2) (2025) 115792.
[37] Z.J. Wang, H. Du, J.H. Gong, S.G. Yang, J.H. Ma, J. Xu, Facile synthesis of hierarchical flower-like γ-AlOOH films *via* hydrothermal route on quartz surface, *Colloids Surf. A Physicochem. Eng. Aspects* 450 (2014) 76–82.
[38] E. Shuang, Q. Wang, K.C. Sheng, X.M. Zhang, Synthesis of Al-modified hydrochar from corn stover for efficient phosphate removal, *J. Environ. Chem. Eng.* 12 (1) (2024) 111725.
[39] J.L. Liu, L.H. Yang, E. Shuang, C.D. Jin, C.X. Gong, K.C. Sheng, X.M. Zhang, Facile one-pot synthesis of functional hydrochar catalyst for biomass valorization, *Fuel* 315 (2022) 123172.
[40] A.M. Thomas, K. Kuntaiah, M.R. Korra, S.S. Nandakishore, Efficient removal of fluoride on aluminum modified activated carbon: an adsorption behavioral study and application to remediation of ground water, *J. Environ. Sci. Health Part A* 58 (1) (2023) 69–80.
[41] B. Xiang, J.X. Tang, X.J. Feng, Y.L. Zhu, Y. Li, T. Tan, Preparation of aluminium-hydroxide-modified diatomite and its fluoride adsorption mechanism, *Sci. Rep.* 13 (1) (2023) 3871.
[42] S. Mukherjee, S. Dutta, S. Ray, G. Halder, A comparative study on defluoridation capabilities of biosorbents: Isotherm, kinetics, thermodynamics, cost estimation, and eco-toxicological study, *Environ. Sci. Pollut. Res. Int.* 25 (18) (2018) 17473–17489.

[43] Z.J. Ma, Q. Zhang, X.Y. Weng, C.Y. Mang, L.W. Si, Z.H. Guan, L. Cheng, Fluoride ion adsorption from wastewater using magnesium(II), aluminum(III) and titanium(IV) modified natural zeolite: Kinetics, thermodynamics, and mechanistic aspects of adsorption, *J. Water Reuse Desalin.* 8 (4) (2018) 479–489.
[44] C.J. Dong, X.M. Wu, Z.Y. Gao, P.L. Yang, M.Y. Ali Khan, A novel and efficient metal oxide fluoride absorbent for drinking water safety and sustainable development, *Sustainability* 13 (2) (2021) 883.
[45] Z. Wang, X.Y. Gu, X.B. Zhang, X. Wang, J.Q. Zhang, Y. Liu, X.N. Tan, Y. Zhao, D.J. Kang, W.S. Guo, H.H. Ngo, New easily recycled carrier based polyurethane foam by loading Al-MOF and biochar for selective removal of fluoride ion from aqueous solutions, *Sci. Total Environ.* 901 (2023) 166312.
[46] N. Tefera, Y. Mulualem, J. Fito, Adsorption of fluoride from aqueous solution and groundwater onto activated carbon of avocado seeds, *Water Conserv. Sci. Eng.* 5 (3) (2020) 187–197.
[47] X.L. Fan, Z. Qian, J.Q. Liu, N. Geng, J. Hou, D.D. Li, Investigation on the adsorption of antibiotics from water by metal loaded sewage sludge biochar, *Water Sci. Technol.* 83 (3) (2021) 739–750.
[48] R. Duan, W. Li, D.X. Chen, T. Cui, T. Xiang, Y. Zhang, H.B. Wang, R. Xu, Co-removal of mercury and organic dye *via* the rectangle-shaped nanosheets loaded hydrochar: surface interactions and DFT calculations, *Sep. Purif. Technol.* 353 (2025) 128553.
[49] J. Petrović, M. Koprivica, M. Ercegović, M. Simić, J. Dimitrijević, M. Bugarčić, S. Trifunović, Synthesis and application of FeMg-modified hydrochar for efficient removal of lead ions from aqueous solution, *Processes* 13 (7) (2025) 2060.
[50] Y.L. Nie, C. Hu, C.P. Kong, Enhanced fluoride adsorption using Al (III) modified calcium hydroxyapatite, *J. Hazard. Mater.* 233-234 (2012) 194–199.
[51] J.B. Chen, R.J. Yang, Z.Y. Zhang, D.Y. Wu, Removal of fluoride from water using aluminum hydroxide-loaded zeolite synthesized from coal fly ash, *J. Hazard. Mater.* 421 (2022) 126817.
[52] X.Y. Sun, C.P. Ke, Q.F. Lu, L. Liang, G.Y. Xie, Adsorption of fluoride ion on Al/La modified acidified attapulgite composite materials, *Sep. Purif. Technol.* 354 (2025) 128791.
[53] S.G. Wang, Y. Ma, Y.J. Shi, W.X. Gong, Defluoridation performance and mechanism of nano-scale aluminum oxide hydroxide in aqueous solution, *J. Chem. Technol. Biotechnol.* 84 (7) (2009) 1043–1050.
[54] B. Wang, L.X. Huo, D.S. Wang, Defluorination behaviors using different types of aluminum salts: the effect of SO_4^{2-}, *Colloids Surf. A Physicochem. Eng. Aspects* 624 (2021) 126768.